QUBIT-RESONATOR SYSTEM AS AN APPLICATION TO QUANTUM COMPUTATION

Ren-Shou Huang

Submitted to the faculty of the Graduate School
in partial fulfillment of the requirements
for the degree
Doctor of Philosophy
in the Department of Physics,
Indiana University

May 2004

Accepted by the Graduate Faculty, Indiana University, in partial fulfillment of the requirements of the degree of Doctor of Philosophy.

Doctoral Committee

Professor Steven M. Girvin (Chairman)

Professor John P. Carini

Professor David V. Baxter

May 14, 2004

Professor Adam Szczepaniak

Abstract

Ren-Shou Huang

Qubit-Resonator System as an Application to Quantum Computation

The recent development of quantum computation has inspired lots of interesting ideas in a variety of fields. It is surprising, and yet not surprising, to see that even systems with very distinct forms can resemble each other in many ways. In our study of a solid state mesocopic system, we found that it bears many features similar to those being seen in cavity quantum electrodynamics in quantum optics. Here the role of the atom is played by a Cooper pair box (CPB), and the cavity is replaced by a transmission line resonator. This combined qubit-resonator system, though its size is much larger than a real atom, still gives us several revelations about fundamental quantum physics.

Due to the interaction between the Cooper pair box and the resonator photon field, their properties both change to reflect each other's character. Like an atom, the

CPB aquires a Lamb shift to its own energy splitting, and the resonator changes its frequency based on the state of the CPB. The latter is especially important, because by taking advatage of this feature we can devise readout schemes that do not perturb the CPB. Since the CPB is practically hidden inside the resonator, the shielding could potentially lead to an enhancement of the qubit lifetime.

Quantum computation requires at least stages of control, operation, and readout. We show that even though the qubit is hidden inside the resonator, we can still control it with standard NMR techniques using microwaves. Furthermore, the resonator itself may also serve as a medium for communicating among multiple qubits and facilitating quantum operations. Therefore, this system, if realized in the experiments, could be a promising candidate for the basic structure of a quantum computer in the future.

Professor Steven M. Girvin
(Chairman)

Professor John P. Carini

Professor David V. Baxter

Professor Adam Szczepaniak

Contents

List of Figures

Chapter 1

Introduction

It has been a long time since physicists thought of the idea of using quantum mechanics as a means to perform computation.[1, 2, 3, 4] However until recently, it was not widely taken seriously. Now this idea has bloomed in many fields such as NMR[5], AMO[6, 7, 8], solid state physics[9, 10], etc. Numerous known systems have been proposed as candidates for qubits.

Here we propose a system for the basic structure of quantum computation. A Cooper pair box as a qubit is placed between a superconducting transmission line and its ground plane, and the energy splitting of the CPB is far detuned from the resonator frequency. In this design the resonator can be used to protect the qubits, for connecting different qubits, and even reading out the states of the qubits. It was some time before we realized that this is in fact a solid state analog of cavity quantum electrodynamics, where a two-level atom is placed inside a resonant cavity. The interaction between the atom and the photon gives rise to many interesting phenomena found in fundamental quantum physics.

Chapter 2 extensively covers the theoretical foundation of one of the primary components, the superconducting transmission line resonator. We start by modeling

the resonator with an infinitesimal lumped element circuit. From this model we are able to derive its simple harmonic oscillator properties by second quantization. In practice, the resonator is capacitively typically coupled to two external leads to conduct incoming and outgoing signals. This system is also treated with the same modeling method and later extended to a theoretical Hamiltonian. Two important results of this coupling are the shift of resonant frequency and the dissipation due to the leakage to the external continua. Since we are going to extract information from the resonator by sending in microwaves, the transmission properties are also investigated using the standard S matrix method as in a scattering problem.

In Chapter 3, we first introduce the qubit, a Cooper pair box, and then derive the interaction between the qubit and resonator once they are coupled together. This leads to the famous Jaynes-Cummings Hamiltonian. We can diagonalize it either exactly with the dressed state picture, or approximately with perturbation theory. We find that the resonator frequency will shift higher or lower depending on the state of the qubit. This phenomenon gives us an advantage to explore two quantum non-demolition qubit readout schemes using the resonator. Another advantage this system provides us is that the qubit's spontaneous emission could be suppressed because the large detuning of the qubit energy splitting from the resonator frequency.

Since all the operations on this system involve microwaves, but the microwave driven Jaynes-Cummings Hamiltonian is not exactly solvable, we are required to numerically simulate it. The method is solving the time evolution of the density matrix. The conjectured system parameters are chosen based on known facts. The microwaves coming from the external transmission line lead are simplified to a direct driven power coupling to the qubit-resonator system. The simulation results correctly

verified our two readout schemes previously devised. Furthermore, we are able to simulate a way to control the state of the qubit with methods similar to those in nuclear magnetic resonance. At the end, a simulation of the Ramsey experiment is also demonstrated.

Chapter 2

Superconducting Transmission Line Resonator

A segment of superconducting transmission line with transverse dimension much smaller than its length can be treated as a 1D harmonic oscillator. Here it will be coupled with two external leads to transmit input and output signals. This system can be solved exactly, and a theoretical model is established. We also calculate the dissipation associated with continua in the leads. We also solve the resonator response to the input microwave as a scattering problem.

2.1 Segment of Transmission Line

2.1.1 First Quantization

When we pass a microwave signal through a transmission line of length L, if the wavelength is much longer than the dimension of the cross section, the charge on the transmission line can, to a good approximation, be considered to be moving in only

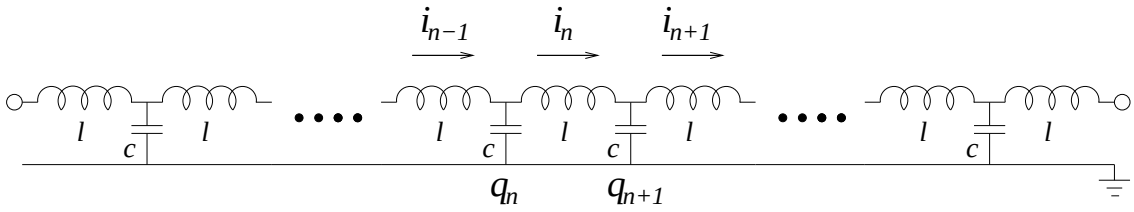

Figure 2.1: Schematic circuit model for the transmission line resonator.

one spatial dimension. Thus we can make an infinitesimal lumped element circuit model for it, as in Fig. (2.1). The Lagrangian of the system is

$$\mathbf{L} = \sum_n \left[\frac{l i_n^2}{2} - \frac{q_n^2}{2c} \right], \tag{2.1}$$

where c is the capacitance of each small capacitor and l is the inductance of each small inductor. Notice that $\dot{q}_n = i_{n-1} - i_n$, so $i_n = -\sum_{m=1}^{n} \dot{q}_m$,

$$\mathbf{L} = \sum_n \left[\frac{l \left(\sum_{m=1}^{n} \dot{q}_m \right)^2}{2} - \frac{q_n^2}{2c} \right]. \tag{2.2}$$

Going from discrete to continuous variables, we define the collective field variable

$$\vartheta(x,t) = \int_{-\frac{L}{2}}^{x} dx' q(x',t), \tag{2.3}$$

where $q(x)$ is the linear charge density. Making the replacements

$$\sum_{m=1}^{n} q_m(t) \longrightarrow \vartheta(x,t), \qquad q_n(t) \longrightarrow q(x,t) = \frac{\partial \vartheta(x,t)}{\partial x}, \tag{2.4}$$

the one-dimensional Lagrangian density becomes

$$\mathcal{L} = \frac{l}{2}\dot{\vartheta}^2 - \frac{1}{2c}\left(\frac{\partial\vartheta}{\partial x}\right)^2. \tag{2.5}$$

Here c and l become the linear density of capacitance and inductance of the transmission line. The Euler-Lagrange equation gives

$$\frac{1}{c}\frac{\partial^2\vartheta}{\partial x^2} - l\frac{\partial^2\vartheta}{\partial t^2} = 0 \tag{2.6}$$

with boundary conditions $\vartheta(-L/2,t) = \vartheta(L/2,t) = 0$ due to charge neutrality. This can be easily solved by separation of variables. The solution is

$$\vartheta(x,t) = \sqrt{\frac{2}{L}}\sum_{j=1}^{j_{\text{cutoff}}}\phi_j(t)\begin{cases}\cos\dfrac{j\pi x}{L}, & j \text{ odd}\\ \sin\dfrac{j\pi x}{L}, & j \text{ even}\end{cases} \tag{2.7}$$

and we also have the mode velocity $v = 1/\sqrt{lc}$, which will be close to the speed of light, and eigenfrequencies $\omega_j = j\pi v/L$. The j_{cutoff} is a cutoff determined by the fact that the structure is not literally one dimensional.

2.1.2 Second Quantization

The time dependent part still has the Euler-Lagrange equation

$$\ddot{\phi}_j + \omega_j^2\phi_j = 0, \tag{2.8}$$

which follows from the Lagrangian density

$$\mathcal{L}_j(\phi_j, \dot{\phi}_j; t) = \frac{l}{2}\dot{\phi_j}^2 - \frac{1}{2c}\left(\frac{j\pi}{L}\right)^2 \phi_j^2. \tag{2.9}$$

From this we can obtain the Hamiltonian as a function of ϕ_j and its canonically conjugate momentum π_j

$$\mathcal{H}_j(\pi_j, \phi_j; t) = \frac{\pi_j^2}{2l} + \frac{1}{2c}\left(\frac{j\pi}{L}\right)^2 \phi_j^2, \qquad \pi_j \equiv \frac{\partial \mathcal{L}_j}{\partial \dot{\phi}_j} = l\dot{\phi}_j. \tag{2.10}$$

Now in order to second quantize the Hamiltonian, we promote the variables ϕ_j and π_j to operators $\hat{\phi}_j$ and $\hat{\pi}_j$ with the quantum commutation relation $[\hat{\phi}_j, \hat{\pi}_{j'}] = i\hbar\delta_{jj'}$. To diagonalize the Hamilitonian, we introduce the bosonic creation and annihilation operators $\hat{a}_j^\dagger$ and $\hat{a}_j$ requiring that $[\hat{a}_j, \hat{a}_{j'}^\dagger] = \delta_{jj'}$. After some algebra we obtain

$$\hat{\phi}_j(t) = \sqrt{\frac{\hbar\omega_j c}{2}}\frac{L}{j\pi}\left[\hat{a}_j(t) + \hat{a}_j^\dagger(t)\right], \tag{2.11}$$

$$\hat{\pi}_j(t) = -i\sqrt{\frac{\hbar\omega_j l}{2}}\left[\hat{a}_j(t) - \hat{a}_j^\dagger(t)\right], \tag{2.12}$$

which, if substituted in Eq. (2.10), gives us the diagonalized Hamiltonian

$$\hat{\mathcal{H}}_j(t) = \hbar\omega_j\left[\hat{a}_j^\dagger(t)\hat{a}_j(t) + \frac{1}{2}\right]. \tag{2.13}$$

Therefore the final solution is

$$\hat{\vartheta}(x,t) = \sum_{j=1}^{j_{\text{cutoff}}} \sqrt{\frac{\hbar\omega_j c}{L}}\frac{L}{j\pi}\left[\hat{a}_j(t) + \hat{a}_j^\dagger(t)\right]\begin{cases} \cos\dfrac{j\pi x}{L}, & j \text{ odd} \\ \sin\dfrac{j\pi x}{L}, & j \text{ even} \end{cases}. \tag{2.14}$$

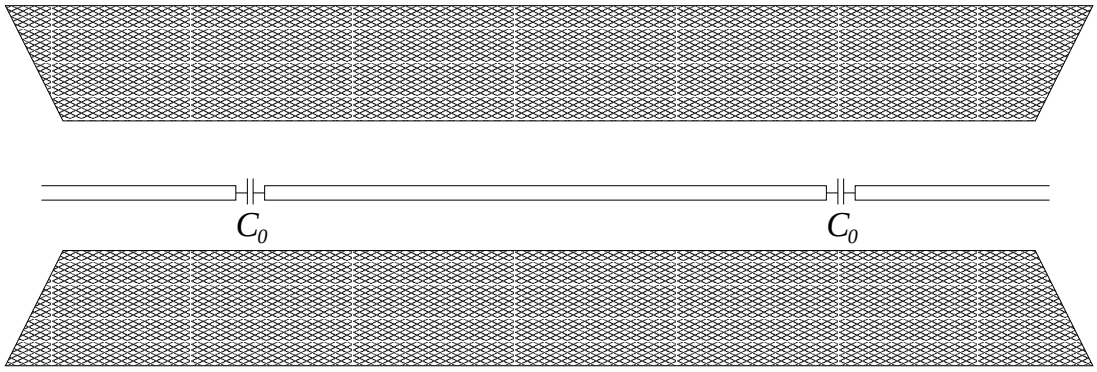

Figure 2.2: The physical view of the transmission line resonator coupling to external leads. The two shaded area are ground planes to keep the resonator well isolated and to form the ground for the coplanar waveguide leads.

A useful quantity that can be derived from this expression is the voltage distribution on the transmission line,

$$\hat{V}(x,t) \equiv \frac{1}{c}\frac{\partial\hat{\vartheta}(x,t)}{\partial x} = \sum_{j=1}^{j_{\text{cutoff}}} \sqrt{\frac{\hbar\omega_j}{Lc}}\left[\hat{a}_j(t) + \hat{a}_j^\dagger(t)\right] \begin{cases} -\sin\dfrac{j\pi x}{L}, & j \text{ odd} \\ +\cos\dfrac{j\pi x}{L}, & j \text{ even} \end{cases} . \quad (2.15)$$

2.2 Transmission Line Resonator Coupling to External Leads

To further investigate the properties of the resonator, we can put a semi-infinite transmission line near each end of the resonator. Here we assume the size of the insulating gap between two adjacent superconducting wires is negligible, but that it still provides only very weak capacitive coupling between the resonator and the

external leads. For simplicity, we assume the leads and resonator have identical inductance and capacitance per unit length. Since for the case we are interested in, the temperature is much lower than all the eigenmode frequencies, we will only focus on one particularly chosen mode of the resonator from now on.

2.2.1 Euler-Lagrange Equation

One way to solve this problem exactly is again through the Euler-Lagrange equation. Including the energy stored in the coupling capacitors, the Lagrangian is

$$\mathcal{L} = \frac{l}{2}\dot{\vartheta}^2 - \frac{1}{2c}\left(\frac{\partial\vartheta}{\partial x}\right)^2 - \frac{\vartheta^2}{2C_0}\left[\delta(x-\frac{L}{2}) + \delta(x+\frac{L}{2})\right], \tag{2.16}$$

where C_0 is the capacitance of the two coupling capacitors which are assumed to be identical. The Euler-Lagrange equation is

$$\frac{1}{c}\frac{\partial^2\vartheta}{\partial x^2} - \frac{\vartheta}{C_0}\left[\delta(x-\frac{L}{2}) + \delta(x+\frac{L}{2})\right] - l\frac{\partial^2\vartheta}{\partial t^2} = 0 \tag{2.17}$$

Here we can see the whole system as an infinitely long transmission line with discontinuities at the coupling capacitors. In fact, the equation is still the same as Eq. (2.6), but now with the boundary conditions determined by the relation between the charges on the coupling capacitors and the voltage drops across them, see Fig. (2.3)

$$\frac{1}{c}\left[\frac{\partial\vartheta\left(-\frac{L}{2}_+\right)}{\partial x} - \frac{\partial\vartheta\left(-\frac{L}{2}_-\right)}{\partial x}\right] = \frac{1}{C_0}\vartheta\left(-\frac{L}{2}_+\right) = \frac{1}{C_0}\vartheta\left(-\frac{L}{2}_-\right), \tag{2.18}$$

$$\frac{1}{c}\left[\frac{\partial\vartheta\left(+\frac{L}{2}_+\right)}{\partial x} - \frac{\partial\vartheta\left(+\frac{L}{2}_-\right)}{\partial x}\right] = \frac{1}{C_0}\vartheta\left(+\frac{L}{2}_+\right) = \frac{1}{C_0}\vartheta\left(+\frac{L}{2}_-\right). \tag{2.19}$$

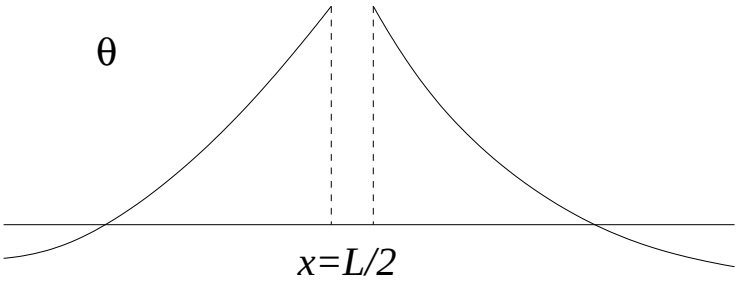

Figure 2.3: Typical behavior of ϑ near one of the coupling capacitor. The spatial gap in between is taken to be zero in the boundary conditions. Therefore the function is continuous but its first derivative is not, due to the finite amount of charge on each plate of the capacitor.

This is analogous to the problem of the Schrödinger equation with a delta function potential. The spatial part of the solution of the symmetric modes is of the form

$$\vartheta_S(x) = \begin{cases} B\cos(kx+\delta_k), & x > L/2 \\ A\cos kx, & -L/2 < x < L/2 \\ B\cos(kx-\delta_k), & x < -L/2 \end{cases} \tag{2.20}$$

The quantity δ_k is the phase difference between the wave functions inside and outside the resonator. Fitting to the boundary conditions we obtain

$$R(k) \equiv \frac{|A|^2}{|B|^2} = \frac{1}{1+\frac{c^2}{k^2C_0^2}\cos^2\frac{kL}{2} - \frac{2c}{kC_0}\sin\frac{kL}{2}\cos\frac{kL}{2}}, \tag{2.21}$$

$$\delta_k = \tan^{-1}\left(\tan\frac{kL}{2} - \frac{c}{kC_0}\right) - \frac{kL}{2}. \tag{2.22}$$

These quantities are plotted in Fig. (2.4) and Fig. (2.5). $R(k)$ is the response inside the resonator when there is an input microwave at frequency $\omega = kv$. In terms of frequency, near the first peak, $\omega \sim \pi v/L$, $R(k)$ can be very well approximated by

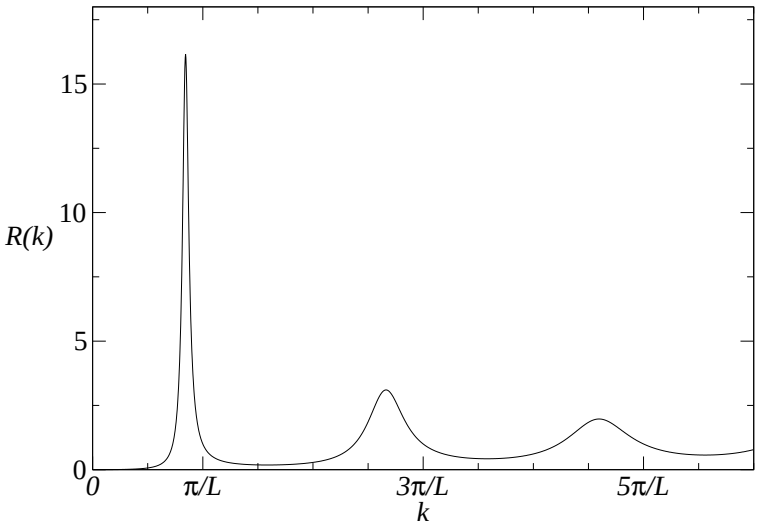

Figure 2.4: Microwave response of the resonator at $Lc/C_0 = 10$. The result shown here is calculated for the symmetric modes, so we can only see peaks near odd multiples of π/L. Notice that they are slightly shifted to the left from their original values.

a Lorentzian function with center ω_R slightly shifted away from the original value $\omega_1 = \pi v/L$,

$$R(\omega = kv) \simeq \frac{2v}{L} \frac{\omega_R/2Q}{(\omega - \omega_R)^2 + (\omega_R/2Q)^2}, \tag{2.23}$$

where Q is by definition equal to the peak frequency divided by FWHM. Fig. (2.6) and Fig. (2.7) show the dependence of the frequency shift $|\omega_R - \omega_1|$ and Q on the parameter Lc/C_0. The downward shift of the frequency occurs because of the capacitive loading of the resonator by the discrete capacitors.

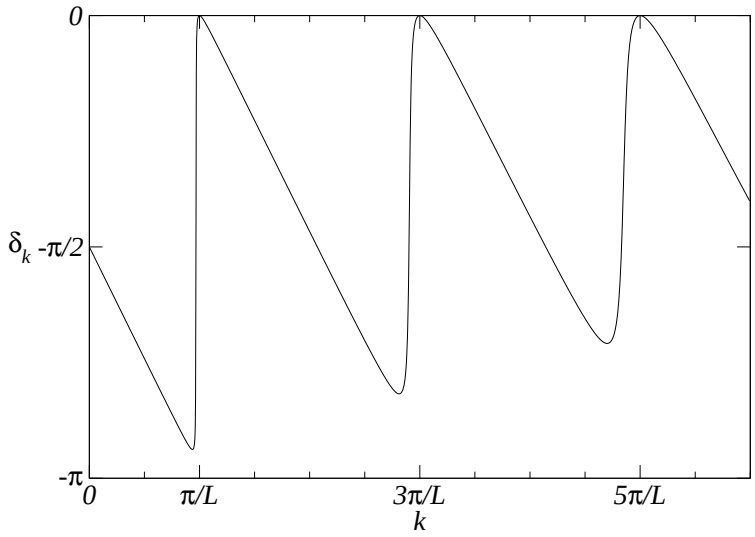

Figure 2.5: The phase shift δ_k as a function of momentum (frequency) for the symmetric modes. As predicted by resonance theory, when the frequency passes through the resonance frequency, the phase shift jumps from nearly $-\pi$ to 0. Here the jump is reduced because of the exaggeratedly heavy damping due to the relatively small value chosen for the control parameter $Lc/C_0 = 60$. In the actual experiments $Lc/C_0 \sim 200 - 1000$ will be used.

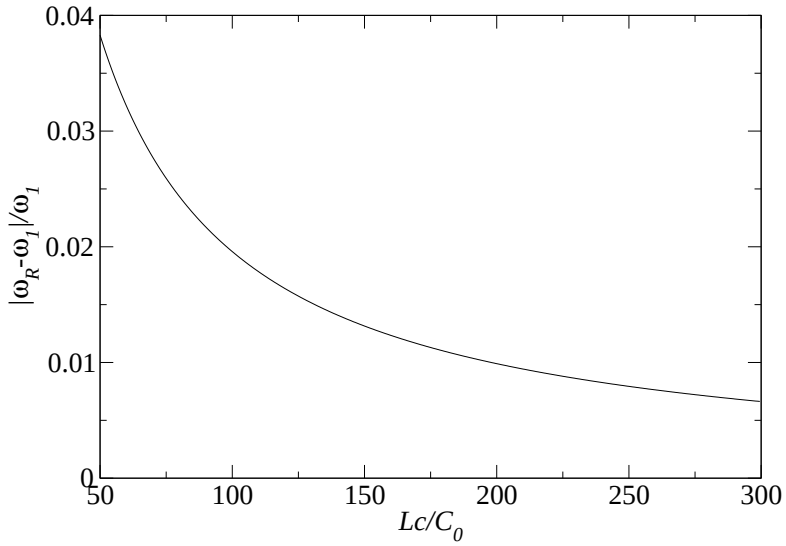

Figure 2.6: Shift of the fundamental mode frequency due to the resonator's coupling to the external leads vs. the control parameter Lc/C_0. It will be shown in Sec. 2.2.2 that in fact $|\omega_R - \omega_1|/\omega_1 \propto C_0/Lc$ when $Lc/C_0 \gg 1$.

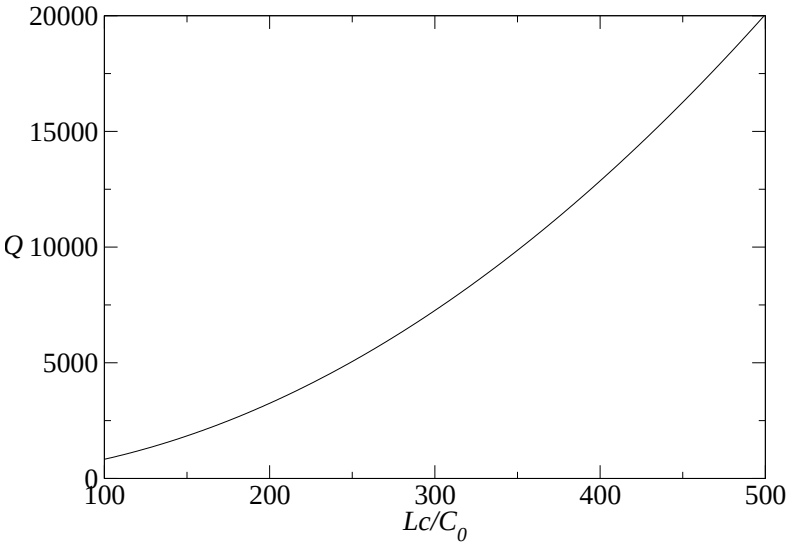

Figure 2.7: Q values extracted from the Lorentzian function used to approximate the peak of the fundamental mode. It will be shown in Sec. 2.3.2 that this is a parabola.

Figure 2.8: Schematic circuit of the effective base Hamiltonian of each section of the transmission lines. Due to the coupling capacitors, their wavefunctions will no longer vanish at the ends. The overlaps of wavefunctions of different sections give rise to the hopping terms of the photons in the effective Hamiltonian.

2.2.2 Theoretical Model

To derive the Hamiltonian for the system, we can start by rewriting the total Lagrangian as

$$\begin{aligned}\mathbf{L}_{\mathrm{TL}} &= \int_{-\infty}^{\infty} dx \left[\frac{l}{2}\dot{\vartheta}^2 - \frac{1}{2c}\left(\frac{\partial\vartheta}{\partial x}\right)^2\right] \\ &\quad -\frac{C_0}{2c^2}\left(\frac{\partial\vartheta(\frac{L}{2}_+)}{\partial x} - \frac{\partial\vartheta(\frac{L}{2}_-)}{\partial x}\right)^2 - \frac{C_0}{2c^2}\left(\frac{\partial\vartheta(-\frac{L}{2}_+)}{\partial x} - \frac{\partial\vartheta(-\frac{L}{2}_-)}{\partial x}\right)^2 .\end{aligned} \tag{2.24}$$

Since in the real experiment the coupling capacitance is very small, we can treat the system as three independent sections with small couplings as perturbations. Further inspection shows that in the coupling energy in Eq. (2.24), there are those square terms involving only one section and also those cross terms that connect two adjacent sections. It is best for us to include all the terms of each section together and treat the cross terms as perturbations. We can see that the frequencies of each section now are different from an ordinary transmission line. To evaluate those eigenfrequencies and wavefunctions we can isolate the section of interest by grounding the other two sections as in Fig. (2.8).

For instance, if we want to calculate the renormalized frequencies of the central section, we can ground the other two. Then all the terms that are left in Eq. (2.24)

involve only the central section. The result, similar as before, is a wave equation with the boundary conditions deduced from Fig. (2.8)

$$\frac{1}{c}\frac{\partial\vartheta_C(-L/2)}{\partial x} = \frac{\vartheta_C(-L/2)}{C_0}, \qquad \frac{1}{c}\frac{\partial\vartheta_C(L/2)}{\partial x} = -\frac{\vartheta_C(L/2)}{C_0}. \tag{2.25}$$

Again we only look at the symmetric fundamental mode. The equation yields a solution to be determined numerically,

$$\tan\frac{kL}{2} = \frac{c}{C_0 k}. \tag{2.26}$$

Its first non-negative solution in the limit $\epsilon = C_0/Lc \ll 1$ obeys,

$$k \sim \frac{\pi}{L}(1-2\epsilon), \tag{2.27}$$

$$\omega = vk \sim \frac{\pi v}{L}(1-2\epsilon). \tag{2.28}$$

Thus the numerical result in Fig. (2.6) is verified.

Applying the same procedures as in Sec. 2.1.2, we arrive at

$$\hat{\vartheta}_C(x,t) = \sqrt{\frac{\hbar\omega c}{L}}\frac{L}{\pi}\cos kx\left[\hat{a}^\dagger(t)+\hat{a}(t)\right]. \tag{2.29}$$

The voltage at the ends is

$$\hat{V}_C\left(\pm\frac{L}{2},t\right) = \frac{1}{c}\frac{\partial\vartheta_C(\pm L/2,t)}{\partial x} = \mp\sqrt{\frac{\hbar\omega}{Lc}}(1-2\epsilon)\left(1-\frac{\pi^2\epsilon^2}{2}\right)\left[\hat{a}^\dagger(t)+\hat{a}(t)\right]. \tag{2.30}$$

The same thing can also be done on the semi-infinite transmission lines on the two

sides. Taking the right-hand side for example, the boundary condition is

$$\frac{1}{c}\frac{\partial\vartheta_R(L/2)}{\partial x} = \frac{\vartheta_R(L/2)}{C_0}, \tag{2.31}$$

which leads to the result

$$\vartheta_R(x,t) = \sum_q \sqrt{\frac{\hbar\omega_q c}{L_{\text{inf}}}}\frac{1}{q}\sin\left[q\left(x-\frac{L}{2}\right)+\delta_q\right]\left[\hat{b}_q^\dagger(t)+\hat{b}_q(t)\right], \tag{2.32}$$

where L_{inf} is the length of the semi-infinit transmission lines, which is, in fact, infinite. The frequency ω_q and the phase shift δ_q are given by

$$\begin{aligned}\omega_q &= vq,\\ \delta_q &= \tan^{-1}\frac{C_0 q}{c}.\end{aligned} \tag{2.33}$$

Although it seems that the coupling capacitor does not cause the frequencies of a semi-infinite transmission line to change, in fact it produces small phase shifts for all the modes that change the originally constant density of states. The voltage at the end is

$$V_R\left(\frac{L}{2},t\right) = \sum_q \sqrt{\frac{\hbar\omega_q}{L_{\text{inf}}c}}\cos\delta_q\left[\hat{b}_q^\dagger(t)+\hat{b}_q(t)\right]. \tag{2.34}$$

When $C_0/Lc \ll 1$, $\cos\delta_q \sim 1$.

Now we can conclude the construction of the theoretical model for the transmission line coupled to two external leads by writing down the Hamiltonian directly from the Lagrangian in Eq. (2.24)

$$\hat{\mathcal{H}}_{\text{TL}} = \hbar\omega\hat{a}^\dagger\hat{a} + \sum_q \hbar\omega_q\hat{b}_{q,L}^\dagger\hat{b}_{q,L} + \sum_q \hbar\omega_q\hat{b}_{q,R}^\dagger\hat{b}_{q,R}$$

$$-\sum_q \lambda_q(\hat{a}^\dagger + \hat{a})(\hat{b}^\dagger_{q,L} + \hat{b}_{q,L}) + \sum_q \lambda_q(\hat{a}^\dagger + \hat{a})(\hat{b}^\dagger_{q,R} + \hat{b}_{q,R}). \quad (2.35)$$

in which the frequencies ω and ω_q are given above, and the new parameters are

$$\lambda_q = C_0\sqrt{\frac{\hbar\omega}{Lc}}\sqrt{\frac{\hbar\omega_q}{L_{\rm inf}c}}(1-2\epsilon)\left(1-\frac{\pi^2\epsilon^2}{2}\right)\cos\delta_q \sim C_0\sqrt{\frac{\hbar\omega}{Lc}}\sqrt{\frac{\hbar\omega_q}{L_{\rm inf}c}}. \quad (2.36)$$

In Eq. (2.35), the interaction part of the Hamiltonian has terms like $\hat{a}\hat{b}_q$ or $\hat{a}^\dagger\hat{b}^\dagger_q$, which have rapidly oscillating time dependence like $e^{\pm i(\omega+\omega_q)t}$. In most cases their contribution can be neglected. By making the *rotating wave approximation* we can drop these terms so that the final Hamiltonian ready to use is

$$\begin{aligned}\hat{\mathcal{H}}_{\rm TL} &= \hbar\omega\hat{a}^\dagger\hat{a} + \sum_q \hbar\omega_q\hat{b}^\dagger_{q,L}\hat{b}_{q,L} + \sum_q \hbar\omega_q\hat{b}^\dagger_{q,R}\hat{b}_{q,R} \\ &\quad -\sum_q \lambda_q(\hat{a}^\dagger\hat{b}_{q,L} + \hat{a}\hat{b}^\dagger_{q,L}) + \sum_q \lambda_q(\hat{a}^\dagger\hat{b}_{q,R} + \hat{a}\hat{b}^\dagger_{q,R}). \end{aligned} \quad (2.37)$$

Notice the different signs of the interactions between the resonator and the leads on two sides. For the fundamental mode, the voltages at the two ends have exactly the same amplitude but opposite signs.

2.3 Dissipation

In the resonator, the dissipation of energy occurs mainly through the coupling to the external leads, assuming that other mechanisms of dissipation are negligible. There are two expressions for this we find useful.

2.3.1 Heisenberg Equations

Here it is more convenient to use the interaction picture. The interaction is

$$\begin{aligned}\tilde{\mathcal{V}}_{\mathrm{TL}} &= -\sum_q \lambda_q(\tilde{a}^\dagger \tilde{b}_{q,L} e^{i(\omega-\omega_q)t} + \tilde{a}\tilde{b}^\dagger_{q,L} e^{i(\omega_q-\omega)t}) \\ &\quad + \sum_q \lambda_q(\tilde{a}^\dagger \tilde{b}_{q,R} e^{i(\omega-\omega_q)t} + \tilde{a}\tilde{b}^\dagger_{q,R} e^{i(\omega_q-\omega)t}). \end{aligned} \tag{2.38}$$

$\tilde{a} = \hat{a}e^{i\omega t}$ is the interaction representation of the annihilation operator, and so are the others.

Now we can write down the Heisenberg equations of motion for the operators,

$$\dot{\tilde{a}} = -\frac{i}{\hbar}[\tilde{a}, \tilde{\mathcal{V}}_{\mathrm{TL}}] = i\sum_q \lambda_q \tilde{b}_{q,L} e^{i(\omega-\omega_q)t} - i\sum_q \lambda_q \tilde{b}_{q,R} e^{i(\omega-\omega_q)t}, \tag{2.39}$$

$$\dot{\tilde{b}}_{q,L} = -\frac{i}{\hbar}[\tilde{b}_{q,L}, \tilde{\mathcal{V}}_{\mathrm{TL}}] = i\lambda_q \tilde{a} e^{i(\omega_q-\omega)t}, \tag{2.40}$$

$$\dot{\tilde{b}}_{q,R} = -\frac{i}{\hbar}[\tilde{b}_{q,R}, \tilde{\mathcal{V}}_{\mathrm{TL}}] = -i\lambda_q \tilde{a} e^{i(\omega_q-\omega)t}. \tag{2.41}$$

Next we integrate the two $\tilde{b}$ equations and plug them into the equation for $\tilde{a}$,

$$\begin{aligned}\dot{\tilde{a}} &= i\sum_q \lambda_q \tilde{b}_{q,L}(0) e^{i(\omega-\omega_q)t} - i\sum_q \lambda_q \tilde{b}_{q,R}(0) e^{i(\omega-\omega_q)t} \\ &\quad - \sum_q \lambda_q^2 \int_0^t dt' \tilde{a}(t') e^{i(\omega-\omega_q)(t-t')} - \sum_q \lambda_q^2 \int_0^t dt' \tilde{a}(t') e^{i(\omega-\omega_q)(t-t')}. \end{aligned} \tag{2.42}$$

The first two terms are the quantum noises, which will be discussed later. For now, they are omitted and set to zero. The two remaining terms are identical,

$$\dot{\tilde{a}} = -2\sum_q \lambda_q^2 \int_0^t dt' \tilde{a}(t') e^{i(\omega-\omega_q)(t-t')}$$

$$\simeq \quad -2\int_0^\infty d\omega_q \rho(\omega_q)\lambda_q^2 \int_0^t dt' \tilde{a}(t') e^{i(\omega-\omega_q)(t-t')}. \tag{2.43}$$

$\rho(\omega_q)$ is the transmission line density of states as a function of frequency. Careful inspection tells us that due to the oscillating exponential, the time integral is significant only around $\omega_q \sim \omega$. If we further assume that the density of states and the coupling parameter vary slowly near ω, we can replace $\rho(\omega_q)$ by a constant ρ_ω and λ_q by a constant λ_ω, and safely move the lower limit of the frequency integral to $-\infty$. It can be simplified to

$$\int_{-\infty}^{\infty} d\omega_q e^{i(\omega-\omega_q)(t-t')} = 2\pi\delta(t-t'). \tag{2.44}$$

This results in[1]

$$\dot{\tilde{a}} = -2\pi\rho_\omega\lambda_\omega^2\tilde{a}(t) \equiv -\frac{\kappa}{2}\tilde{a}(t). \tag{2.45}$$

The above simplifications are called the *Weisskopf-Wigner approximation*[11]. The resonator photon number expectation value obeys

$$\langle\hat{a}^\dagger(t)\hat{a}(t)\rangle = \langle\tilde{a}^\dagger(t)\tilde{a}(t)\rangle \propto e^{-\kappa t}. \tag{2.46}$$

We can see that the photons in the resonator, *i.e.* the energy, leak out at rate $\kappa = 2\times 2\pi\rho_\omega\lambda_\omega^2$ as given by Fermi's golden rule.

[1]Notice the upper limit of the time integral in Eq. (2.43) is t, which includes only half of the delta function. Also notice that the approximations we have made effectively ignore the real part of the photon self-energy in the resonator and hence miss the resonance frequency shift due to the coupling to the continua.

2.3.2 Perturbation Theory

Another approach to the dissipation problem is to calculate the self energy of the resonator photon in perturbation theory. The first non-vanishing correction is in the second order,

$$\begin{aligned}\Sigma_a^{(2)}(\omega) &= 2\sum_q \frac{\lambda_q^2}{\omega-\omega_q+i\eta} \simeq \frac{2C_0^2\omega}{Lc^2L_{\rm inf}}\sum_q \frac{\omega_q\cos^2\delta_q}{\omega-\omega_q+i\eta} \\ &= \frac{2C_0^2\omega}{Lc^2L_{\rm inf}}\sum_q \frac{\omega_q}{\omega-\omega_q+i\eta}\frac{1}{1+(C_0\omega_q/cv)^2},\end{aligned} \tag{2.47}$$

where the λ_q is given by Eq. (2.36). The momentum sum can be replaced by a frequency integral

$$\frac{1}{L_{\rm inf}}\sum_q \longrightarrow \int_0^\infty \frac{d\omega_q}{\pi v}. \tag{2.48}$$

In order to carry out the integration, we have to make the same change as in Weisskopf-Wigner approximation by lowering the lower limit to $-\infty$. Keep in mind that the resonator frequency is $\omega/v \simeq j\pi/L$ depending on the chosen mode, the contour integral yields

$$\Sigma_a^{(2)}(\omega) = -2\pi j\left(\frac{v}{L}\right)^2\frac{1}{cv/C_0-i\omega} \sim -2\omega\frac{C_0}{Lc} - 2\pi ij\left(\frac{C_0}{Lc}\right)^2\omega, \tag{2.49}$$

because $cv/C_0 \gg \omega$.

The real part of the self energy reproduces the result in Eq. (2.28), which gives a downward shift of resonant frequency. However, if these result of Eq. (2.28) and the real part of Eq. (2.49) add up, the sum would be twice the amount obtained from the Euler-Lagrange equation plotted in Fig. (2.6). The reason for this discrepancy is still

a mystery to us.

The imaginary part means that the peak around ω is broadened in the spectrum. Also notice it is linear in ω, as expected for an ohmic bath, which means that for the fundamental mode $j = 1$,

$$Q \equiv \frac{\omega}{\kappa} \equiv \frac{\omega}{-2\mathrm{Im}\left[\Sigma_a^{(2)}\right]} = \frac{1}{4\pi}\left(\frac{Lc}{C_0}\right)^2, \tag{2.50}$$

whose dependence on the control parameter Lc/C_0 has been plotted in Fig. (2.7) and they agree perfectly.

2.4 Transmission Properties

When a microwave pulse comes in from one of the external leads, it can either transmit to the other side or be reflected back. Thus in nature this can be viewed as a 1-D scattering problem, and the key to this problem is the *S matrix*

$$S_{fi} = \lim_{t\to\infty} \langle \psi_f | U(t/2, -t/2) | \psi_i \rangle, \tag{2.51}$$

which is the transition amplitude of an initial state in the remote past moving to a final state in the distant future. In our case the initial state would be one of the Fourier components of the incoming wave, and the final state is that of the outgoing wave. Following the derivation in Merzbacher[12],

$$S_{fi} = \delta_{fi} - 2\pi i \delta(E_f - E_i) T_{fi}. \tag{2.52}$$

The first term on the right is the trivial part of the matrix element meaning that the incoming wave is unaffected by the local scattering potential. In the second term, T_{fi} is called the transition matrix and obeys the self-consistent equation

$$T = V + VGT, \tag{2.53}$$

where V is the scattering potential and G is the Green's function.

Before we proceed to calculate the S matrix, we should clarify what the states really look like. Assume that the input microwave comes from the left, and we know the eigenfunction of the semi-infinite transmission line is given by the spatial part of Eq. (2.32). However, the sine function has a right-moving (incoming) part and a left-moving (outgoing) part. Although this seems to give a stationary state, in fact, if a right-moving wave packet is created in the past, then in the future after it hits the wall it will become inverted and bounce back. Therefore the eigenstates used in the bracket are the same regardless of time, yet the wave packet they make up looks very different in the past and in the future.

The S matrix with the initial state being a photon on the left side can have two possible outcomes depending on whether the final state is a photon on the left (reflected) or on the right (transmitted). If calculated up to second order, they are

$$S_{f_L i} = \delta_{k_f,k_i} - 2\pi i\delta(E_f - E_i)\frac{\lambda_{k_f}\lambda_{k_i}}{E_i - \omega + i\kappa/2}, \tag{2.54}$$

$$S_{f_R i} = -2\pi i\delta(E_f - E_i)\frac{\lambda_{k_f}\lambda_{k_i}}{E_i - \omega + i\kappa/2}. \tag{2.55}$$

Here we choose the radiative-corrected resonator photon propagator to include the

higher order corrections[13]. κ, the same as in Eq. (2.45) and Eq. (2.50), is the decay rate of the discrete resonator levels associated with the two continua of the leads. The Dirac delta can be transformed to a Kronecker delta times the density of states, because there are no degeneracies in the semi-infinite transmission line mode. Here we invoke the expression for κ in Eq. (2.45). Since $2\pi\rho(\omega)\lambda_\omega^2$ itself is the decay rate to the left side, if as we assumed earlier that the two sides are identical, that would be exactly half of the total decay rate. Thus the S matrix elements become

$$S_{f_L i} = \delta_{k_f,k_i}\left[1 - \frac{i\kappa/2}{(E_i-\omega)+i\kappa/2}\right] = \delta_{k_f,k_i}\frac{E_i-\omega}{(E_i-\omega)+i\kappa/2}, \tag{2.56}$$

$$S_{f_R i} = \delta_{k_f,k_i}\frac{-i\kappa/2}{(E_i-\omega)+i\kappa/2}. \tag{2.57}$$

It can be verified that the sum of these two S matrix elements squared is unity, which conserves the total flux. Also the Breit-Wigner form correctly predicts the phase shift of the outgoing waves.

One particular example worth looking at is when $E_i = \omega$, so that the input microwave frequency matches the resonator frequency. The S matrix element for reflection vanishes, which means that the input microwave is completely transmitted to the right side in this special case.

Chapter 3

Qubit-Resonator System

In the concept of quantum computing, the information is stored in qubits. Currently there are many experimentally realizable solid state systems that can serve this purpose. Those made of superconducting materials can be divided into several categories, charge qubits[10], flux qubits[14], phase qubits[15, 16], and Saclay qubit[17]. Here we will focus on a Cooper pair box as a charge qubit, but the same principle can be applied to others as well.

One qubit is certainly not enough for information processing. For several qubits to work together, a medium to communicate the information is required. The medium we choose is the transmission line resonator. It provides many advantages such as isolation of the qubit, free readout scheme, etc, which will be discussed in this chapter.

3.1 Cooper Pair Box

A Cooper pair box is basically a superconducting island connected to the ground via a Josephson junction, as in Fig. (3.1).

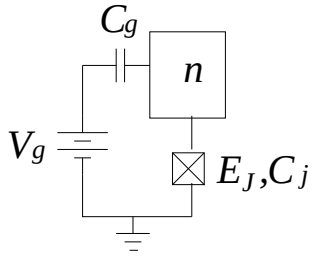

Figure 3.1: Schematic picture of a Cooper pair box. The large square is the superconducting island. The small square is the Josephson junction.

3.1.1 Charging Energy

Assume the island has n excess Cooper pairs and potential V,

$$-2ne = C_g(V - V_g) + C_j V, \tag{3.1}$$

$$\Rightarrow \qquad V(n) = \frac{C_g V_g - 2ne}{C_\Sigma}, \tag{3.2}$$

where $C_\Sigma = C_g + C_j$. Therefore the energy required for Δn Cooper pairs to move onto an island with inital n excess Cooper pairs is

$$E(n+\Delta n) - E(n) = -2e \int_0^{\Delta n} V(n+n')dn' = \frac{2e^2\Delta n^2 + 4e^2 n\Delta n - 2eC_g V_g \Delta n}{C_\Sigma}. \tag{3.3}$$

To make this look better, set

$$E(0) = \frac{2e^2}{C_\Sigma}\left(\frac{C_g V_g}{2e}\right)^2. \tag{3.4}$$

So that for arbitrary n, the charging energy

$$E(n) = 4E_C(n - n_g)^2, \tag{3.5}$$

where the single electron charging energy is defined as $E_C \equiv e^2/2C_\Sigma$ and the gate charge as $n_g \equiv C_g V_g/2e$.

3.1.2 Josephson Tunnelling

The Hamiltonian describing Josephson tunnelling in the most common notation is[18]

$$\hat{\mathcal{H}}_J = -|\varphi_1, \varphi_2\rangle E_J \cos(\varphi_1 - \varphi_2)\langle\varphi_1, \varphi_2|, \tag{3.6}$$

where φ_1 and φ_2 are the phases on the two sides of the junction, and E_J is the Josephson energy.

For our purpose, it is more useful to transform it into the number basis. Multiply the Hamiltonian by two closures

$$\begin{aligned}
\hat{\mathcal{H}}_J &= -\sum_{n_1,n_2,n_3,n_4} |n_1, n_2\rangle\langle n_1, n_2|\varphi_1, \varphi_2\rangle E_J \cos(\varphi_1 - \varphi_2)\langle\varphi_1, \varphi_2|n_3, n_4\rangle\langle n_3, n_4| \\
&= -E_J \sum_{n_1,n_2,n_3,n_4} \int_0^{2\pi} \frac{d\varphi_1}{2\pi} e^{-i(n_1-n_3)\varphi_1} \int_0^{2\pi} \frac{d\varphi_2}{2\pi} e^{-i(n_2-n_4)\varphi_2} \\
&\qquad \times \frac{e^{i(\varphi_1-\varphi_2)} + e^{i(\varphi_2-\varphi_1)}}{2} |n_1, n_2\rangle\langle n_3, n_4| \\
&= -\frac{E_J}{2} \sum_{n_1,n_2} (|n_1, n_2\rangle\langle n_1 - 1, n_2 + 1| + |n_1, n_2\rangle\langle n_1 + 1, n_2 - 1|).
\end{aligned} \tag{3.7}$$

Here the state vectors like $|n_1, n_2\rangle$ denote the number state on the two sides of the junction. The result means that Josephson tunnelling is simply Cooper pairs jumping from one side to the other one by one.

Since one side of the junction in a Cooper pair box is the ground, due to its reservoir nature, we can forget about its number state and keep track of only the

number of excess Cooper pairs on the island. Thus for us,

$$\hat{\mathcal{H}}_J = -\frac{E_J}{2}\sum_n (|n\rangle\langle n+1| + |n+1\rangle\langle n|). \tag{3.8}$$

3.1.3 Coulomb Blockade

Combining Eq.(3.4) and Eq.(3.8), we arrive at the Hamiltonian of the Cooper pair box

$$\hat{\mathcal{H}}_{\mathrm{CPB}} = \sum_n \left[4E_C(n-n_g)^2|n\rangle\langle n| - \frac{E_J}{2}(|n\rangle\langle n+1| + |n+1\rangle\langle n|)\right]. \tag{3.9}$$

In real experiments, E_C and E_J have to be larger than k_BT to lower the impact of thermal fluctuations, and E_C must be smaller than the gap energy of the superconductor to avoid unwanted quasi-particles. Also we choose to work in the charge limit $E_C > E_J$ so that the charging energy is dominant.

Numerically diagonalizing the Hamiltonian yields the eigenenergies as functions of the gate charge, which are shown in Fig. (3.2). We can see that the degeneracies where the two charging energy parabolas of adjacent numbers cross are lifted by Josephson tunnelling by an amount E_J. Since the behavior is periodic in gate voltage, we can focus on the range $m \leq n_g \leq m+1$ as in Fig. (3.3). Notice that the ground state of the Cooper pair box, as the gate voltage increases, shifts from m to $m+1$. The average number of excess Cooper pairs on the island is plotted against gate voltage in Fig. (3.4). The sharp rise of the staircase is due to the discreteness of Cooper pair number, i.e. the Cooper pair has to overcome the blockade of charging energy to hop on or off the island. The rapid variation of the Cooper pair number near the degeneracy point $n_g = m + 0.5$ provides us a great property to exploit this

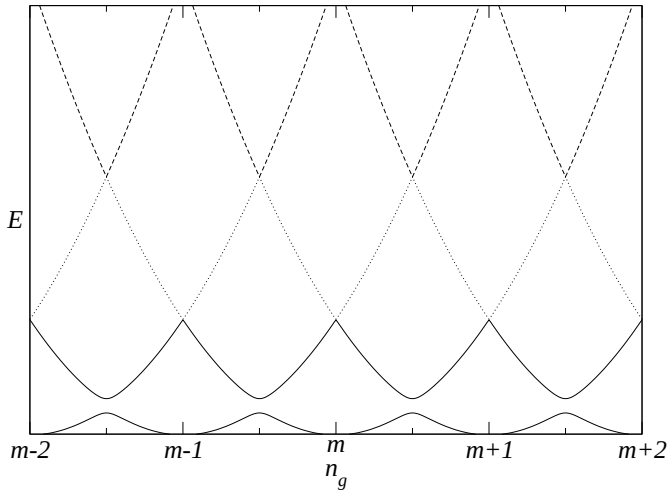

Figure 3.2: Eigenenergies of some lowest states of a Cooper pair box as a function of gate charge. Notice they were originally charging energy parabolas where the crossings between different number states are lifted by Josephson tunnelling.

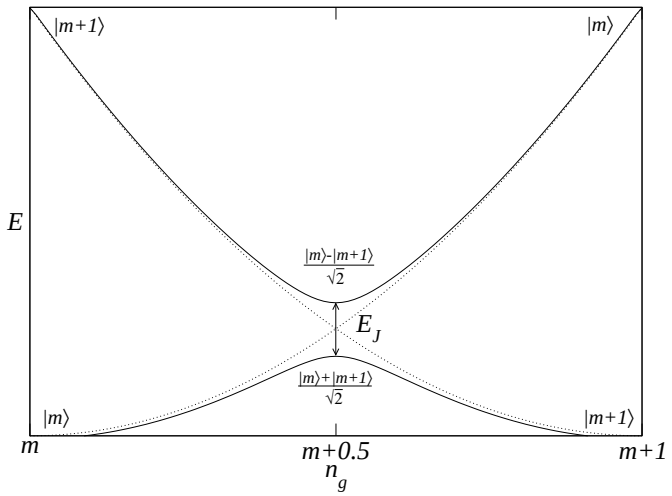

Figure 3.3: Magnification of the region between $m < n_g < m + 1$ in Fig. (3.2). The solid lines are the eigenenergies of the two lowest states, and dotted lines are the charging energies of charge states $|m\rangle$ and $|m + 1\rangle$ without Josephson tunnelling. At $n_g = m + 0.5$, the energy splitting is exactly E_J, and the states are equal mixtures of $|m\rangle$ and $|m + 1\rangle$.

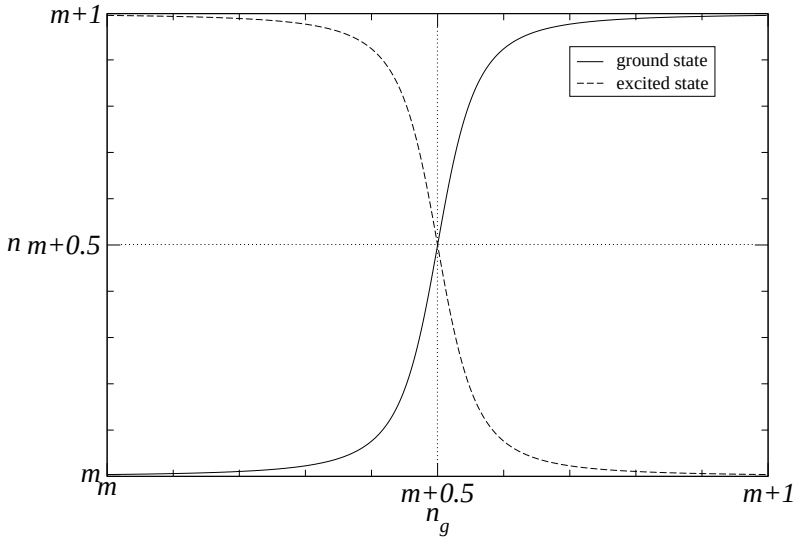

Figure 3.4: Number of Cooper pairs on the island in the ground and excited states as functions of gate charge.

as a macroscopic two-level system, which in our case is the qubit. Its coherence was first demonstrated by Nakamura, *et al.*[10]

If we focus only on the two lowest levels, we can rewrite the qubit Hamiltonian in the spin notation

$$\hat{\mathcal{H}}_{\mathrm{qb}} = 2E_C(1-2n_g)\hat{\sigma}^z - \frac{E_J}{2}\hat{\sigma}^x, \tag{3.10}$$

where the diagonal term $4E_C n_g^2$ has been dropped.

3.2 Cooper Pair Box Coupling to a Resonator

A Cooper pair box whose size is on the scale of micrometers can be placed between the transmission line and the ground plane, where the Cooper pairs on it can Josephson tunnel to the ground plane while remaining capacitively coupled to the

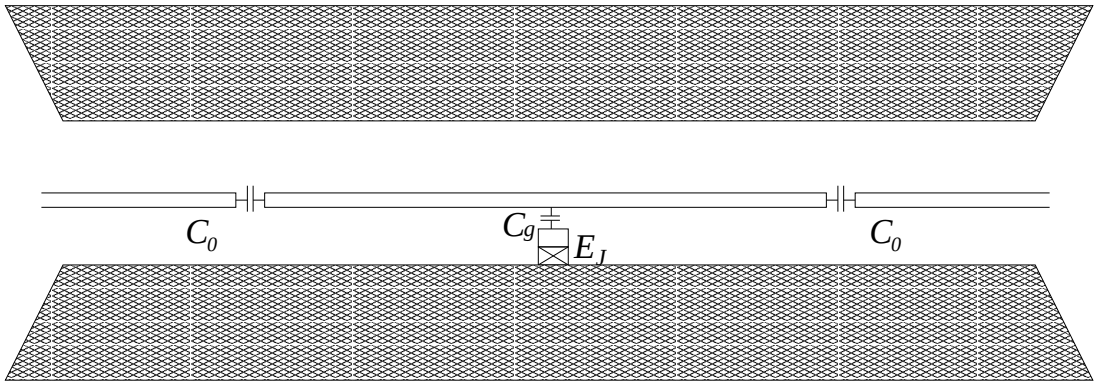

Figure 3.5: Physical view of the system. The size of the Cooper pair box is exaggerated here. Usually a Cooper pair box is in the order of μm, while a transmission line resonator of $\sim$ 10GHz frequency has a length of centimeters. The gap between the center conductor and the ground plane is approximately 10μm.

resonator. The center line of the resonator acts as the gate electrode. A DC voltage on the center conductor of the transmission line couples through C_0 to the resonator and hence to the qubit through the gate capacitance. For our purposes, we tune the Cooper pair box to stay at its degeneracy point $n_g = 0.5$ and put it at the center of the resonator. Because the voltage of the fundamental mode vanishes at the center, we choose the one resonator mode of interest to be the first excited mode, $\omega = \omega_2$. Therefore, the gate voltage of the Cooper pair box includes the AC voltage of each mode of the resonator in addition to the DC voltage V_g. The extra term due to the interaction between the resonator and the Cooper pair box coming out of Eq. (3.10) is

$$\begin{aligned} \hat{\mathcal{H}}_{\text{int}} &= -\frac{2E_C C_g}{e}\hat{\sigma}^z\sqrt{\frac{\hbar\omega_2}{Lc}}(\hat{a}_2^\dagger + \hat{a}_2)\cos\frac{2\pi x}{L} \\ &= -\frac{eC_g}{C_\Sigma}\hat{\sigma}^z\sqrt{\frac{\hbar\omega_2}{Lc}}(\hat{a}_2^\dagger + \hat{a}_2). \end{aligned} \tag{3.11}$$

From now on, we will drop the resonator mode index. The Hamiltonian of the whole system for the special case that the qubit is at the charge degeneracy point is

$$\begin{aligned}\hat{\mathcal{H}} &= -\frac{E_J}{2}\hat{\sigma}^x + \hbar\omega\hat{a}^\dagger\hat{a} - g\hat{\sigma}^z(\hat{a}^\dagger + \hat{a}) + \sum_q \hbar\omega_q b_{q,L}^\dagger b_{q,L} + \sum_q \hbar\omega_q b_{q,R}^\dagger b_{q,R} \\ &\quad + \sum_q \lambda_q(\hat{a}^\dagger b_{q,L} + \hat{a}b_{q,L}^\dagger) + \sum_q \lambda_q(\hat{a}^\dagger b_{q,R} + \hat{a}b_{q,R}^\dagger), \end{aligned} \tag{3.12}$$

where

$$g \equiv \frac{eC_g}{C_\Sigma}\sqrt{\frac{\hbar\omega}{Lc}}. \tag{3.13}$$

To further simplify the expression, we rotate the axes of the spin directions so that

$$\hat{\sigma}^z \longrightarrow \hat{\sigma}^x, \qquad \hat{\sigma}^x \longrightarrow -\hat{\sigma}^z. \tag{3.14}$$

Then the first three terms become

$$\frac{E_J}{2}\hat{\sigma}^z + \hbar\omega\hat{a}^\dagger\hat{a} - g\hat{\sigma}^x(\hat{a}^\dagger + \hat{a}) \simeq \frac{E_J}{2}\hat{\sigma}^z + \hbar\omega\hat{a}^\dagger\hat{a} - g(\hat{a}^\dagger\hat{\sigma}^- + \hat{a}\hat{\sigma}^+), \tag{3.15}$$

which is the famous *Jaynes-Cummings Hamiltonian*. Here again we make the rotating wave approximation to get rid of the rapidly rotating terms like $\hat{a}\hat{\sigma}^-$. At last, the Hamiltonian for the whole system is

$$\begin{aligned}\hat{\mathcal{H}} &= \frac{E_J}{2}\hat{\sigma}^z + \hbar\omega\hat{a}^\dagger\hat{a} - g(\hat{a}^\dagger\hat{\sigma}^- + \hat{a}\hat{\sigma}^+) + \sum_q \hbar\omega_q \hat{b}_{q,L}^\dagger \hat{b}_{q,L} + \sum_q \hbar\omega_q \hat{b}_{q,R}^\dagger \hat{b}_{q,R} \\ &\quad + \sum_q \lambda_q(\hat{a}^\dagger \hat{b}_{q,L} + \hat{a}\hat{b}_{q,L}^\dagger) + \sum_q \lambda_q(\hat{a}^\dagger \hat{b}_{q,R} + \hat{a}\hat{b}_{q,R}^\dagger). \end{aligned} \tag{3.16}$$

Here we neglect the internal dissipation mechanism directly associated with the Cooper pair box, for the reason that it is well hidden inside the resonator. Also

$E_J \simeq \omega$ must be satisfied so that other modes of the resonator and higher excitations in the Cooper pair box can be neglected.

A similar system can be found in cavity quantum electrodynamics[19, 20], where a two-level atom passes through a resonant cavity. The key parameters are the atom-photon interaction constant g, the cavity photon decay rate κ as discussed in Sec. 2.3, and the atom decay rate γ since the atom still couples to environment directly. In order to see the most interesting quantum behavior, the strong coupling limit must be reached $g \gg \kappa, \gamma$[21].

3.3 Frequency Shift

One special feature of the qubit-resonator system is the shift of the resonator frequency induced by the presence of the qubit. There are two ways to explain it that we find useful.

3.3.1 Dressed State Picture

The dressed states are made of the energy levels of the bare Hamiltonian without the qubit-resonator interaction and dissipation, Eq. (3.15). With the interaction between the qubit and the resonator turned on, the original states $|\uparrow, n\rangle$ and $|\downarrow, n+1\rangle$ can be diagonalized to $|+, n\rangle$ and $|-, n\rangle$, as in Fig. (3.6). The energy splittings between them change from $\Delta \equiv E_J - \hbar\omega$ to $\sqrt{\Delta^2 + 4(n+1)g^2}$. Assuming $E_J > \hbar\omega$ and $\Delta \gg 2\sqrt{n+1}g$ from now on, the states $|+, n\rangle$ are pretty much $|\uparrow, n\rangle$ and $|-, n\rangle$ are very close to $|\downarrow, n+1\rangle$. Therefore, the qubit states $|\uparrow\rangle$ and $|\downarrow\rangle$ can still be

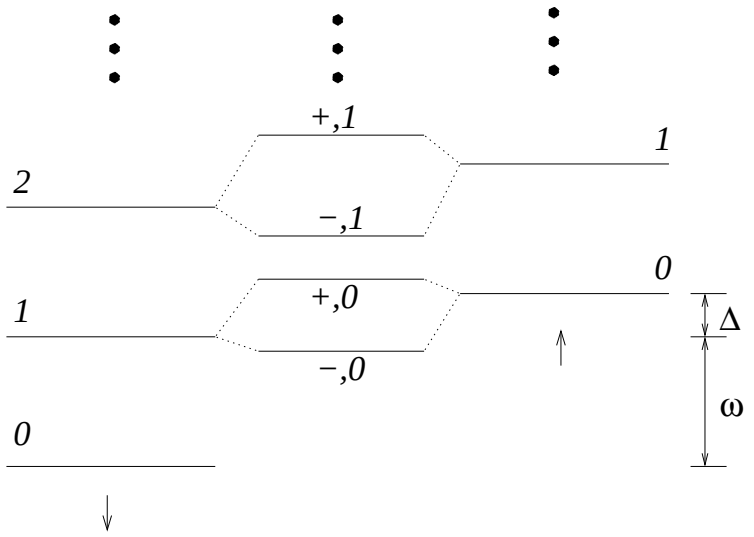

Figure 3.6: Dressed state picture of the qubit-resonator system. The left and the right columns are the energy states of the qubit and the resonator photons without the interaction. The central column is the diagonalized energy eigenstates with the interaction turned on. The energy splittings between the + and − states of the same number n are $\sqrt{\Delta^2 + 4(n+1)g^2}$

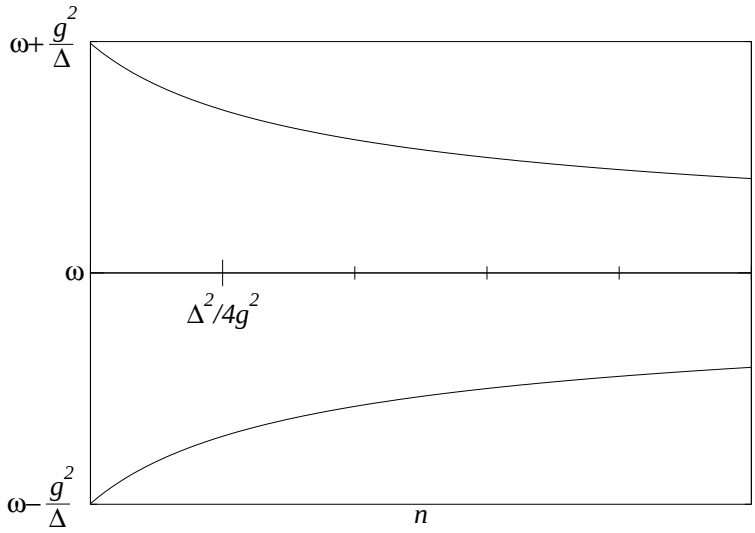

Figure 3.7: Dependence of frequency shift on photon number. The upper curve and the lower curve represent the energy differences of + states and − states of adjacent photon numbers. These two curves will eventually meet at ω as $n \to \infty$.

identified by the new states $|+\rangle$ and $|-\rangle$. The energy required to create one more photon is

$$\begin{aligned} E_{+,n+1} - E_{+,n} &= \hbar\omega + \sqrt{\Delta^2 + 4(n+2)g^2} - \sqrt{\Delta^2 + 4(n+1)g^2} \sim \hbar\omega + \frac{g^2}{\Delta}, \\ E_{-,n+1} - E_{-,n} &= \hbar\omega - \sqrt{\Delta^2 + 4(n+1)g^2} + \sqrt{\Delta^2 + 4ng^2} \sim \hbar\omega - \frac{g^2}{\Delta}. \end{aligned} \tag{3.17}$$

They are plotted in Fig. (3.7). We can notice in the graph that when the photon number is small, the photon energies, *i.e.* frequencies, split into two values depending on the state of the qubit. The splitting becomes smaller as the photon number grows larger.

3.3.2 Effective Hamiltonian

In the limit where g is small, the qubit-resonator interaction in the Jaynes-Cummings Hamiltonian, Eq. (3.15), can be treated perturbatively. Although this is only an approximation, in certain cases it is more useful than the exact expressions obtained in the dressed state picture. The effective Hamiltonian calculated up to the second order is

$$\begin{aligned}\hat{\mathcal{H}}_{\text{eff}} &\simeq \frac{E_J}{2}\hat{\sigma}^z + \hbar\omega\hat{a}^\dagger\hat{a} + \frac{g^2\hat{a}^\dagger\hat{a}\hat{\sigma}^-\hat{\sigma}^+}{\hbar\omega - E_J} + \frac{g^2\hat{a}\hat{a}^\dagger\hat{\sigma}^+\hat{\sigma}^-}{E_J - \hbar\omega} \\ &= \left(E_J + \frac{g^2}{\Delta}\right)\frac{\hat{\sigma}^z}{2} + \left(\hbar\omega + \frac{g^2}{\Delta}\hat{\sigma}^z\right)\hat{a}^\dagger\hat{a} + \frac{g^2}{2\Delta}. \end{aligned} \tag{3.18}$$

The last term is a constant which can be dropped. We see that two correction terms arise due to the coupling between the qubit and the resonator. One is the frequency shift of the resonator photon discussed in previous section, but the second order perturbation theory only recovers the part of the qubit state dependent correction in the expansion that is independent of photon number. The other term is the Lamb shift of the qubit energy. The same approximation can also be made by expanding the unitary transformation with the operator $\hat{U} = \exp[(g/\Delta)(\hat{a}\hat{\sigma}^+ - \hat{a}^\dagger\hat{\sigma}^-)]$.

3.3.3 Readout Scheme

The shift of frequencies provides us with a great property to exploit. From it we are able to devise two quantum non-demolition (QND) readout schemes that require no additional devices attached to the Cooper pair box.

Quantum Non-Demolition Measurement

A general QND measurement must satisfy certain conditions. Here we follow the discussion in [11]. For a system S to be measured by a probe P via their interaction I, the Hamiltonian is

$$\hat{\mathcal{H}} = \hat{\mathcal{H}}_{\mathrm{S}} + \hat{\mathcal{H}}_{\mathrm{P}} + \hat{\mathcal{H}}_{\mathrm{I}}. \tag{3.19}$$

Now consider the case where we want to know the system observable $\hat{O}_S$ by measuring the probe observable $\hat{O}_P$. Their behavior is governed by the equation of motion

$$\dot{\hat{O}} = -\frac{i}{\hbar}[\hat{O}, \hat{\mathcal{H}}]. \tag{3.20}$$

A measurement is QND type when the following criteria are met

- For the information of $\hat{O}_S$ to be obtained, $\hat{\mathcal{H}}_I$ must be a function of $\hat{O}_S$

$$\frac{\partial \hat{\mathcal{H}}_I}{\partial \hat{O}_S} \neq 0. \tag{3.21}$$

- Because the probe observable $\hat{O}_P$ is used to measure the system S, it cannot be a constant of motion, *i.e.*

$$[\hat{O}_P, \hat{\mathcal{H}}_I] \neq 0. \tag{3.22}$$

- The system observable $\hat{O}_S$ should not change, with or without its coupling to the probe,

$$[\hat{O}_S, \hat{\mathcal{H}}_S] = [\hat{O}_S, \hat{\mathcal{H}}_I] = 0. \tag{3.23}$$

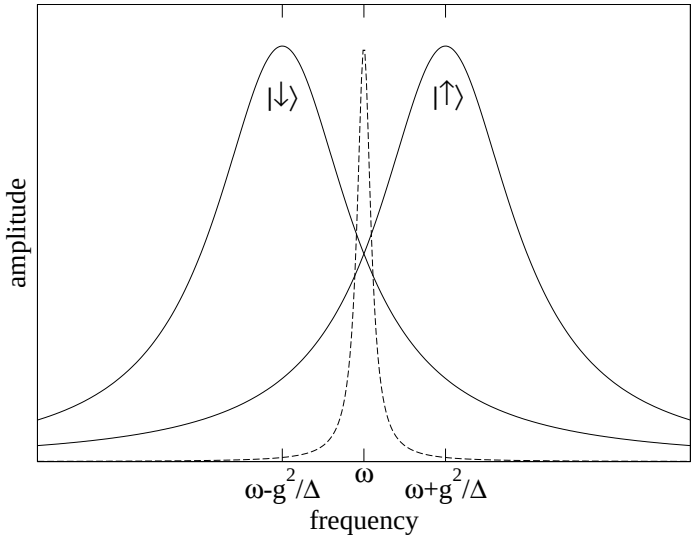

Figure 3.8: Spectral view of the phase measurement. The two solid lines are what the spectrum would be if the qubit is in $|\uparrow\rangle$ or $|\downarrow\rangle$. The dashed line is the spectral density of the input microwave pulse, which is very long compared to the decay rate κ. Because the phase shift of the transmitted microwave is determined by the relative position of the input microwave to the spectrum, the output phase shift will have different signs giving information about the qubit state.

Phase Measurement

Applying the same spirit to the effective Hamiltonian Eq. (3.18), if we want to know the state of the qubit (system) $\hat{O}_S = \hat{\sigma}^z$, we can choose to measure an observable of the resonator (probe),

$$\hat{O}_P \propto (\hat{a}^\dagger + \hat{a}), \tag{3.24}$$

which, if properly normalized, tells us the phase of the resonator photons. In the actual experiment, we can send in microwave signals at the bare resonator frequency. Because the peak of the resonator spectrum has been shifted higher or lower per the qubit state, the phase shift of the output signal gives us the information on the qubit state. A pictorial explanation is shown in Fig. (3.8). The amount of phase shifted is roughly

$$\delta\theta = \tan^{-1}\frac{2g^2}{\kappa\Delta} \sim \pm\frac{2g^2}{\kappa\Delta}. \tag{3.25}$$

The phase measurement is to a good approximation QND in the limit where g is small so that Eq. (3.18) is valid and condition Eq. (3.23) is obeyed. But even in a true QND measurement, it should not be understood that the state of the system is unchanged after the measurement. In fact, it is only the system observable that is unchanged, the state of the system is still affected by the measurement. Here if the qubit is in a superposition of its two eigenstates, it will be strongly dephased in this readout scheme. That is $\langle\sigma^x\rangle$ and $\langle\sigma^y\rangle$ will be changed even if $\langle\sigma^z\rangle$ remains unaffected.

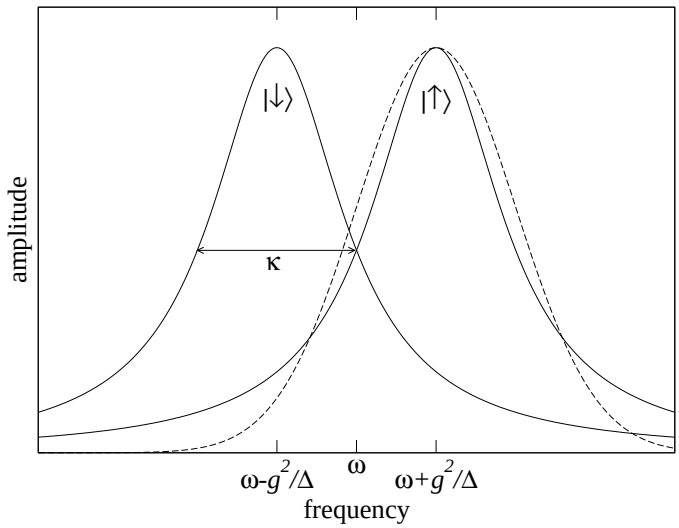

Figure 3.9: Spectral view of the transmission measurement. The input microwave frequency is centered on one of the shifted resonator frequencies. As we can see, the number of photons transmitted at a particular frequency depends on the state of the qubit. But for this method to work, the FWHM must be small enough to resolve the two different peaks, $\kappa < 2g^2/\Delta$. The width of the input microwave pulse can be as large as the width of the each peak for fast measurement.

Transmission Measurement

The other way to measure the state of the qubit is by passing a microwave at the frequency of one of the shifted resonator frequencies. As long as the frequency splitting $2g^2/\Delta$ is larger than the width of the resonator spectrum κ, the shifted frequencies can be easily discerned. A graph is drawn in Fig. (3.9) to explain this. Apparently this is also a QND measurement. Note that this strong coupling condition can be achieved at fixed g by making κ small enough.

No matter which readout scheme is used, the signals on the two external leads are those being measured after all. The reason why the discussion here only refers to the resonator photons is because the photon field superposed on the input signals outside the resonator is simply linearly proportional to that inside, as can be seen from the equation of motion,

$$\dot{\tilde{b}}_q = -i\lambda_q \tilde{a} e^{i(\omega_q - \omega)t}. \tag{3.26}$$

What the effective Hamiltonian tells us is that in this limit the system behaves like an ordinary resonator with two different frequencies depending on the qubit state.

3.4 Qubit Lifetime Enhancement

The Cooper pair box is well hidden inside the space between the transmission line and ground plane. The ground plane, which acts simultaneously as a thermal and Cooper pair reservoir, has a dimension much larger than both the Cooper pair box and the transmission line. It should introduce negligible fluctuations to the qubit. Here we want to include noises intrinsic to the system, such as quasi-particles, defects,

charges or phonons in the substrate, etc., all in a qubit decay rate γ, and we are going to further assume γ is small, $\gamma < \kappa$, because we believe that those noise sources seldom have a strong effect on the energy scale of our system. Therefore the most important factor is the spontaneous decay and the noise through the transmission line resonator.

3.4.1 Direct Coupling

To understand the protection provided by the transmission line and the ground plane, we must first understand what happens without them. For a qubit of energy difference E_J directly coupling to a noise source from a continuum via a capacitor C_g, the Hamiltonian is

$$\hat{\mathcal{H}}_{\text{direct}} = \frac{E_J}{2}\hat{\sigma}^z + \sum_\alpha \epsilon_\alpha |\alpha\rangle\langle\alpha| + \frac{eC_g}{C_\Sigma}\hat{\sigma}^x\hat{V}, \tag{3.27}$$

where C_Σ is the total capacitance, and $\hat{V}$ is the voltage operator of the continuum. The qubit decay rate is given by Fermi's golden rule,

$$\begin{aligned}
\frac{1}{T_{10}} &= \frac{2\pi}{\hbar}\sum_\alpha \text{Tr}_\gamma \left\{ \left| \langle \downarrow \alpha | \frac{eC_g}{C_\Sigma}\hat{\sigma}^x\hat{V} | \uparrow \gamma \rangle \right|^2 \right\} \delta(\epsilon_\alpha - \epsilon_\gamma - E_J) \\
&= \frac{2\pi}{\hbar}\left(\frac{eC_g}{C_\Sigma}\right)^2 \frac{1}{\mathcal{Z}} \sum_{\alpha,\gamma} e^{-\beta\epsilon_\gamma} \left| \langle\alpha|\hat{V}|\gamma\rangle \right|^2 \delta(\epsilon_\alpha - \epsilon_\gamma - E_J) \\
&= \left(\frac{eC_g}{\hbar C_\Sigma}\right)^2 \frac{1}{\mathcal{Z}} \sum_{\alpha,\gamma} e^{-\beta\epsilon_\gamma} \int_{-\infty}^{\infty} dt e^{i\frac{E_J}{\hbar}t} \langle\gamma|\hat{V}(t)|\alpha\rangle\langle\alpha|\hat{V}(0)|\gamma\rangle \\
&= \left(\frac{eC_g}{\hbar C_\Sigma}\right)^2 S_V(\frac{E_J}{\hbar}),
\end{aligned} \tag{3.28}$$

where S_V is the noise voltage spectrum as a function of angular frequency.

3.4.2 Indirect Coupling through the Resonator

Here the qubit does not directly couple to the noise source; its connection to the noise in the external leads is through the resonator. Adopting the result in Sec. 2.2.1, the noise voltage spectrum inside the resonator seen by the qubit should be multiplied by the factor $R(\omega)$. Therefore the decay rate here is

$$\frac{1}{T_1} = \left(\frac{eC_g}{\hbar C_\Sigma}\right)^2 \frac{2v}{L} \frac{\kappa/2}{\Delta^2 + (\kappa/2)^2} S_V(\frac{E_J}{\hbar}). \tag{3.29}$$

We can see that the main difference between Eq. (3.29) and Eq. (3.28) is a Lorentzian factor representing the filtering of the noise by the resonator. In the limit $\Delta \gg \kappa$, the expression for T_1 becomes

$$\frac{1}{T_1} \simeq \left(\frac{eC_g}{\hbar C_\Sigma}\right)^2 \frac{v\kappa}{L\Delta^2} S_V(\frac{E_J}{\hbar}). \tag{3.30}$$

When the factor $v\kappa/L\Delta^2 \ll 1$, the noise induced decay is strongly reduced.

3.4.3 Spontaneous Decay Rate

An useful expression for the spontaneous decay rate can be easily obtained by substituting in the vacuum noise of the transmission line. From Eq. (2.15), we can write down the vacuum noise spectrum at one end of a semi-infinite long transmission line

$$S_{V0}(\omega) = \int_{-\infty}^{\infty} dt e^{i\omega t} \langle \hat{V}(t)\hat{V}(0)\rangle. \tag{3.31}$$

The correlation function at finite temperature is

$$\begin{aligned}\langle \hat{V}(t)\hat{V}(0)\rangle &= \sum_{q=1}^{\infty} \frac{\hbar\omega_q}{L_{\rm inf}c}\langle \hat{b}_q^\dagger(t)\hat{b}_q(0) + \hat{b}_q(t)\hat{b}_q^\dagger(0)\rangle \\ &= \sum_{q=1}^{\infty} \frac{\hbar\omega_q}{L_{\rm inf}c}[n_B(\hbar\omega_q)e^{i\omega_q t} + (n_B(\hbar\omega_q)+1)e^{-i\omega_q t}]. \end{aligned} \tag{3.32}$$

Thus, the spectral function of the vacuum noise in the limit $L_{\rm inf} \to \infty$ is

$$\begin{aligned} S_{V0}(\omega) &= \sum_{q=1}^{\infty} \frac{2\pi\hbar\omega_q}{L_{\rm inf}c}[n_B(\hbar\omega_q)\delta(\omega+\omega_q) + (n_B(\hbar\omega_q)+1)\delta(\omega-\omega_q)] \\ &\longrightarrow 2Z\hbar\int_0^\infty d\omega_q\omega_q[n_B(\hbar\omega_q)\delta(\omega+\omega_q) + (n_B(\hbar\omega_q)+1)\delta(\omega-\omega_q)] \\ &= 2Z\hbar\omega[\theta(\omega)(n_B(\hbar\omega)+1) - \theta(-\omega)n_B(-\hbar\omega)], \end{aligned} \tag{3.33}$$

where $Z = \sqrt{l/c} = 1/vc$ is the impedance of the transmission line. In the low temperature limit $k_BT \ll \hbar\omega$,

$$S_{V0}(\omega) \to 2Z\hbar\omega\theta(\omega) \tag{3.34}$$

Therefore the spontaneous decay rate is

$$\frac{1}{T_1}\Big|_{\rm S} = \left(\frac{eC_g}{\hbar C_\Sigma}\right)^2 \frac{v\kappa}{L\Delta^2}\cdot\frac{1}{2}S_{V0}(\frac{E_J}{\hbar}) = \left(\frac{eC_g}{C_\Sigma}\sqrt{\frac{\hbar\omega}{Lc}}\right)^2 \frac{\kappa}{\Delta^2} = \frac{g^2\kappa}{\Delta^2}. \tag{3.35}$$

The extra factor of one half is because from the Cooper pair box's point of view, it sees two transmission lines in parallel.

Another approach to the spontaneous decay is made by looking at the dressed state picture. For $\Delta \gg 2g$, $|\uparrow,0\rangle \simeq |+,0\rangle$. The state initially in $|+,0\rangle$ now has a

chance to decay to the ground state $|\downarrow, 0\rangle$ by leaking a photon out of the resonator. The only difference between this process and the decaying from $|\downarrow, 1\rangle$ to $|\downarrow, 0\rangle$, which gives the decay rate κ, is the matrix element. Therefore,

$$\frac{1}{T_1}\Big|_{\mathrm{S}} = \frac{|\langle\downarrow, 0|\hat{a}|+, 0\rangle|^2}{|\langle\downarrow, 0|\hat{a}|\downarrow, 1\rangle|^2} \cdot \kappa = |\langle\downarrow, 0|\hat{a}|+, 0\rangle|^2\kappa \simeq \frac{g^2\kappa}{\Delta^2}. \tag{3.36}$$

We can interpret this in perturbation theory as saying that the Cooper pair box excitation spends a fraction g^2/Δ^2 of its time as a photon and the photon decay rate is κ.

However, the purpose of this discussion is not about seeing the life time of the qubit to be enhanced this long, instead, it is to show that the qubit plus resonator system can significantly reduced the noise from to the external leads to effect the qubit so that we can see the other noise in play.

Chapter 4

Microwave Driven Qubit-Resonator System

The response of the qubit-resonator system to the input microwave signals is the key to the understanding of the information contained in the system. Because the problem itself cannot be solved analytically, we apply certain numerical methods to obtain meaningful results. We demonstrate some of the basic elements of quantum computation such as coherent control and readout.

4.1 System Parameters

The main energy scales of this system are determined by the resonator frequency ω, the Josephson energy E_J and charging energy E_C of the Cooper pair box, but E_C is not directly relevant at the charge degeneracy point. To get rid of the quasi-particles, ω must be smaller than the gap energy of the superconducting material. For typical conventional superconductor used in photo-lithography like Nb, which at 300mK has gap energy $\sim$ 1.5meV, it should be pretty safe to choose $\omega = 2\pi \times 10$GHz. This

Parameters	Values $(2\pi \times 10\text{GHz})$
ω	1
E_J	1.1
Δ	0.1
g	5×10^{-3}
κ	10^{-4}
γ	0

Table 4.1: Typical realistic parameters of the qubit-resonator system. All the numbers are in the unit of angular frequency for the convenience of numerical evaluation.

results in a centimeters long transmission line if ω is the first harmonic mode. Since the Josephson junction used in the experiment has a SQUID-like structure, E_J can be tuned by changing the magnetic flux through the junction. It is a variable to be determined later.

The next important numbers are the coupling parameter g and the resonator relaxation rate κ. To reach the strong coupling limit, it is required that $g \gg \kappa$. It has been demonstrated that a superconducting transmission line resonator can have a Q value as high as 10^6[22]. Although high Q seems plausible for minimizing the dissipation, it also limits the measurement speed. Therefore it is best to choose κ to be only slightly smaller than the frequency shift g^2/Δ. The coupling energy g is basically controlled by the capacitance ratio C_g/C_Σ and can be as large as $2\pi \times 50$MHz. So if we choose the detuning $\Delta = 2\pi \times 1$GHz, that gives us $g^2/\Delta = 2\pi \times 2.5$MHz. Thus it is sufficient to choose $\kappa = 2\pi \times 1$MHz, $Q = 10^4$. All the important parameters are tabulated in Table (4.1)[23]

Another quantity worth mentioning is the enhanced spontaneous decay rate discussed in Sec. 3.4.3,

$$\frac{g^2\kappa}{\Delta^2} = 2\pi \times 2.5 \times 10^{-7}\text{GHz}, \tag{4.1}$$

which corresponds to the qubit life time about $\sim 64\mu$s, much longer than the latest observed value.

4.2 Numerical Model

The Hamiltonian for the qubit-resonator system driven by microwaves of frequency ω_l on the left feed line is

$$\begin{aligned}\hat{\mathcal{H}} &= \frac{E_J}{2}\hat{\sigma}^z + \hbar\omega\hat{a}^\dagger\hat{a} - g(\hat{a}^\dagger\hat{\sigma}^- + \hat{a}\hat{\sigma}^+) + \sum_q \hbar\omega_q\hat{b}^\dagger_{q,L}\hat{b}_{q,L} + \sum_q \hbar\omega_q\hat{b}^\dagger_{q,R}\hat{b}_{q,R} \\ &+ \sum_q \lambda_q(\hat{a}^\dagger\hat{b}_{q,L} + \hat{a}\hat{b}^\dagger_{q,L}) + \sum_q \lambda_q(\hat{a}^\dagger\hat{b}_{q,R} + \hat{a}\hat{b}^\dagger_{q,R}) \\ &+ \sum_q (\alpha(t)\hat{b}^\dagger_{q,L}e^{-i\omega_l t} + \alpha^*(t)\hat{b}_{q,L}e^{i\omega_l t}),\end{aligned} \tag{4.2}$$

where $\alpha(t)$ is a complex time-dependent function with units of energy which describes the amplitude of the microwave drive.

We can see that this dynamical system cannot be solved analytically. For numerical computation, it is required to get rid of the infinite degrees of freedom of the two continua. The interactions involved are the driving field and dissipation mechanism. For convenience, this is a good time to switch to the interaction representation. The interaction is

$$\tilde{\mathcal{V}}(t) = -g(\tilde{a}\tilde{\sigma}^+ e^{i(E_J-\omega)t} + \tilde{a}^\dagger\tilde{\sigma}^- e^{i(\omega-E_J)t})$$

$$
\begin{aligned}
&+\sum_q \lambda_q(\tilde{a}^\dagger \tilde{b}_{q,L} e^{i(\omega-\omega_q)t} + \tilde{a}\tilde{b}^\dagger_{q,L} e^{i(\omega_q-\omega)t}) \\
&+\sum_q \lambda_q(\tilde{a}^\dagger \tilde{b}_{q,R} e^{i(\omega-\omega_q)t} + \tilde{a}\tilde{b}^\dagger_{q,R} e^{i(\omega_q-\omega)t}) \\
&+\sum_q (\alpha(t)\tilde{b}^\dagger_{q,L} e^{i(\omega_q-\omega_l)t} + \alpha^*(t)\tilde{b}_{q,L} e^{i(\omega_l-\omega_q)t}) \qquad (4.3)
\end{aligned}
$$

The equations of motion for the operators are

$$\dot{\tilde{a}} = ig\tilde{\sigma}^- e^{i(\omega-E_J)t} - i\sum_q \lambda_q \tilde{b}_{q,L} e^{i(\omega-\omega_q)t} - i\sum_q \lambda_q \tilde{b}_{q,R} e^{i(\omega-\omega_q)t}, \qquad (4.4)$$

$$\dot{\tilde{b}}_{q,L} = -i\lambda_q \tilde{a} e^{i(\omega_q-\omega)t} - i\alpha(t) e^{i(\omega_q-\omega_l)t}, \qquad (4.5)$$

$$\dot{\tilde{b}}_{q,R} = -i\lambda_q \tilde{a} e^{i(\omega_q-\omega)t}. \qquad (4.6)$$

If we integrate the $\dot{\tilde{b}}$ equations and substitute them into the first equation and make the Weisskopf-Wigner approximation for the dissipation terms while neglecting all quantum noise contributions we have

$$\dot{\tilde{a}} = ig\tilde{\sigma}^- e^{i(\omega-E_J)t} - \frac{\kappa}{2}\tilde{a} - \sum_q \lambda_q e^{i(\omega-\omega_l)t} \int_0^t dt' \alpha(t') e^{i(\omega_l-\omega_q)(t-t')}. \qquad (4.7)$$

For the frequency sum in the last term on the right hand side we can make the Weisskopf-Wigner approximation again and obtain

$$\dot{\tilde{a}} = ig\tilde{\sigma}^- e^{i(\omega-E_J)t} - \frac{\kappa}{2}\tilde{a} - \pi\lambda_l \rho_l \alpha(t) e^{i(\omega-\omega_l)t}, \qquad (4.8)$$

where ρ_l is the density of states of the left transmission line at frequency ω_l. In the end the system can be simplified to a qubit coupled to the resonator photon field and being directly driven by the microwave source with damping characterized by a dissipation rate κ.

4.3 Density Matrix Formalism

The numerical calculation is based on the equation of motion of the density matrix in the interaction picture[11],

$$\dot{\hat{\rho}} = -\frac{i}{\hbar}[\hat{\rho}, \tilde{\mathcal{V}}]. \tag{4.9}$$

This equation can be solved by iteration, substituting in

$$\hat{\rho}(t) = \hat{\rho}(t_0) - \frac{i}{\hbar}\int_{t_0}^{t} dt'[\hat{\rho}(t'), \tilde{\mathcal{V}}(t')], \tag{4.10}$$

so that Eq. (4.9) becomes

$$\dot{\hat{\rho}}(t) = -\frac{i}{\hbar}[\hat{\rho}(t_0), \tilde{\mathcal{V}}(t)] - \frac{1}{\hbar^2}\int_{t_0}^{t} dt'[[\hat{\rho}(t'), \tilde{\mathcal{V}}(t')], \tilde{\mathcal{V}}(t)]. \tag{4.11}$$

To obtain the exact solution the iteration must go on, but for our purposes it is sufficient to stop here and replace the t_0 in the first term on the right hand side with t, because in numerical computation the time step must be small. The t_0 in the lower limit of the integral in the second term will be shown to be unimportant later. In our case the system of interest is only the qubit and the resonator mode. The continua on the transmission lines on the two sides are to be traced out. Therefore the equation we really want to evaluate is

$$\mathrm{Tr}_C\{\dot{\hat{\rho}}(t)\} = -\frac{i}{\hbar}\mathrm{Tr}_C\{[\hat{\rho}(t), \tilde{\mathcal{V}}(t)]\} - \frac{1}{\hbar^2}\int_{t_0}^{t} dt'\mathrm{Tr}_C\{[[\hat{\rho}(t'), \tilde{\mathcal{V}}(t')], \tilde{\mathcal{V}}(t)]\}, \tag{4.12}$$

where the index C means the trace is over the continua. The reason for this expansion to second order in $\tilde{\mathcal{V}}$ and tracing out is to get rid of the continua while keeping the

key physics.

Since the interaction $\tilde{\mathcal{V}}$ is small, which means that the entanglement between the system and the continua is also small, and we know from previous section that the response of the external continua to the resonator is linear, therefore we can set the density matrix ρ to be separable for all time,

$$\hat{\rho}(t) \simeq \hat{\rho}_S(t) \otimes \hat{\rho}_C(t), \tag{4.13}$$

where the indices S and C denote the system, qubit and resonator, and the continua on the side transmission lines respectively. Also notice that the quantum noise in the continua is ignored because the drive amplitude is assumed to be much larger than the noise amplitude. Then the equation becomes

$$\dot{\hat{\rho}}_S(t) = -\frac{i}{\hbar}\mathrm{Tr}_C\{[\hat{\rho}_S(t)\otimes\hat{\rho}_C(t), \tilde{\mathcal{V}}(t)]\} - \frac{1}{\hbar^2}\int_{t_0}^{t} dt' \mathrm{Tr}_C\{[[\hat{\rho}_S(t')\otimes\hat{\rho}_C(t'), \tilde{\mathcal{V}}(t')], \tilde{\mathcal{V}}(t)]\}. \tag{4.14}$$

Substituting Eq. (4.3) into the equation, but as explained above, in the second order expansion only those terms related to the continua are included, we have

$$\begin{aligned}
\dot{\hat{\rho}}_S(t) \;=\; & \frac{ig}{\hbar}[\hat{\rho}_S(t), \tilde{a}\tilde{\sigma}^+]e^{i(E_J-\omega)t} - \frac{i}{\hbar}\sum_q \lambda_q[\hat{\rho}_S(t), \tilde{a}]\langle \tilde{b}^\dagger_{q,L} + \tilde{b}^\dagger_{q,R}\rangle e^{i(\omega_q-\omega)t} \\
& -\frac{1}{\hbar^2}\int_{t_0}^{t} dt' \sum_q \lambda_q^2 \Big[(\tilde{a}\tilde{a}^\dagger\hat{\rho}_S(t') - \tilde{a}^\dagger\hat{\rho}_S(t')\tilde{a})(\langle \tilde{b}^\dagger_{q,L}\tilde{b}_{q,L}\rangle + \langle \tilde{b}^\dagger_{q,R}\tilde{b}_{q,R}\rangle)e^{i(\omega_q-\omega)(t-t')} \\
& \qquad +(\tilde{a}^\dagger\tilde{a}\hat{\rho}_S(t') - \tilde{a}\hat{\rho}_S(t')\tilde{a}^\dagger)(\langle \tilde{b}_{q,L}\tilde{b}^\dagger_{q,L}\rangle + \langle \tilde{b}_{q,R}\tilde{b}^\dagger_{q,R}\rangle)e^{i(\omega-\omega_q)(t-t')}\Big] \\
& -\frac{1}{\hbar^2}\int_{t_0}^{t} dt' \sum_q \lambda_q \Big[\alpha(t)(\tilde{a}^\dagger\hat{\rho}_S(t') - \tilde{a}^\dagger\hat{\rho}_S(t'))e^{i(\omega-\omega_l)t}\langle \tilde{b}^\dagger_{q,L}\tilde{b}_{q,L}\rangle e^{i(\omega_q-\omega)(t-t')} \\
& \qquad +\alpha^*(t)(\tilde{a}\hat{\rho}_S(t') - \hat{\rho}_S(t')\tilde{a})e^{i(\omega_l-\omega)t}\langle \tilde{b}_{q,L}\tilde{b}^\dagger_{q,L}\rangle e^{i(\omega-\omega_q)(t-t')}\Big] + \text{h.c.}
\end{aligned} \tag{4.15}$$

Because we are working at the zero temperature limit, the ensemble averages $\langle\tilde{b}\rangle$, $\langle\tilde{b}^\dagger\rangle$, and $\langle\tilde{b}^\dagger\tilde{b}\rangle$ all vanish. For the remaining terms with $\langle\tilde{b}\tilde{b}^\dagger\rangle = 1$ the Weisskopf-Wigner approximation is made again and the final equation for $\hat{\rho}_S(t)$ is

$$\begin{aligned}\dot{\hat{\rho}}_S(t) &= -\frac{i}{\hbar}[\hat{\rho}_S(t), -g(\tilde{a}\tilde{\sigma}^+ e^{i(E_J-\omega)t} + \tilde{a}^\dagger\tilde{\sigma}^- e^{i(\omega-E_J)t}) \\ &\qquad -i\pi\lambda_l\rho_l(\alpha(t)\tilde{a}^\dagger e^{i(\omega-\omega_l)t} + \alpha^*(t)\tilde{a}e^{i(\omega_l-\omega)t})] \\ &\quad -\frac{\kappa}{2}(\tilde{a}^\dagger\tilde{a}\hat{\rho}_S(t) - 2\tilde{a}^\dagger\hat{\rho}_S(t)\tilde{a} + \hat{\rho}_S(t)\tilde{a}^\dagger\tilde{a}). \qquad (4.16)\end{aligned}$$

The result is the same as derived in previous section. The system can be thought of as a qubit-resonator system being directly driven by microwaves and having dissipation rate κ. The difference is that now in the density matrix formalism the dissipation requires a special treatment as in the last term.

4.4 Simulation Result

The implementation of the numerical calculation is by solving the density matrix equation Eq. (4.16) with the fourth order Runge-Kutta method. Due to the limitation of the available computer memory, the largest dimension of the matrix can only be 120×120. The system density matrix is the direct product of qubit density matrix and resonator density matrix,

$$\hat{\rho}_S = \hat{\rho}_{\text{qb}} \otimes \hat{\rho}_{\text{res}}. \qquad (4.17)$$

Because the qubit has 2 states, the maximum allowable photon number is $120 \div 2 = 60$. If we assume the photon number distribution inside the resonator is close to a coherent state, to be safe the highest average photon count in the simulation should not exceed

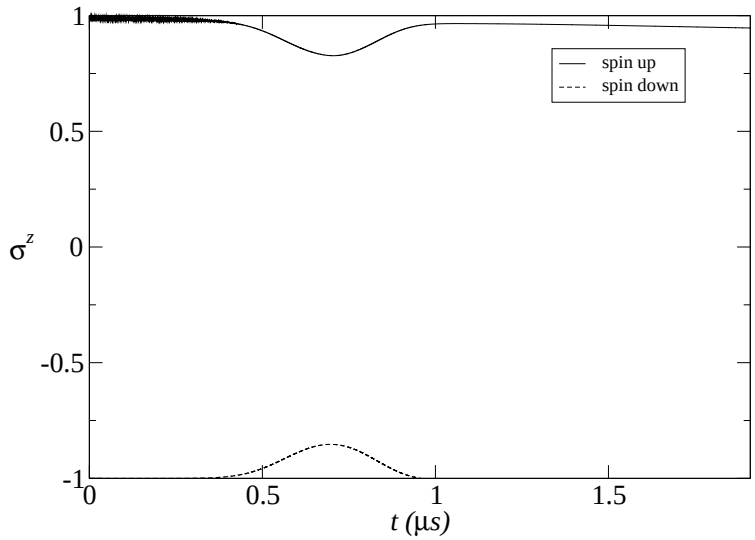

Figure 4.1: Evolution of the box states initiallly at $|\uparrow\rangle$ and $|\downarrow\rangle$ in a phase measurement.

50. It is so chosen because the photon shot noise adds a $\pm\sqrt{n}$ deviation, and $50+\sqrt{50}$ is still less than 60. Also since in the equation the fastest oscillating frequency is Δ, the time step must be smaller than $1/\Delta$.

A Gaussian wave pulse is used for the driving microwave. The width of the pulse is chosen to be on the order of κ to optimize between efficiency and resolution, because although a pulse with a narrower band width resolves better, it takes longer time, and vice versa. Due to the filtering of resonator, κ is the maximum allowable band width. Since it is sufficient to resolve the frequency splitting, this is the fastest way to make a measurement. The amplitude of the pulse is determined by the result of the simulation to satisfy the upper bound for the average photon number.

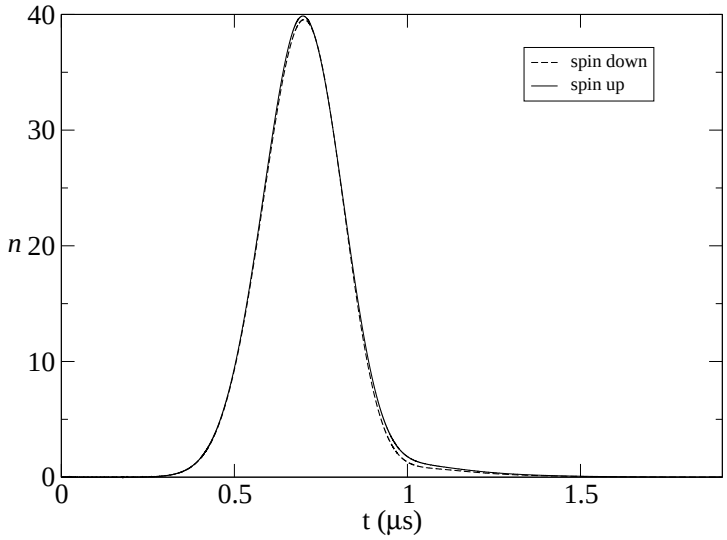

Figure 4.2: Photon number inside the resonator as functions of time in a phase measurement. Notice that the two curves are almost identical indicating that in a phase measurement the information is not carried by the photon number.

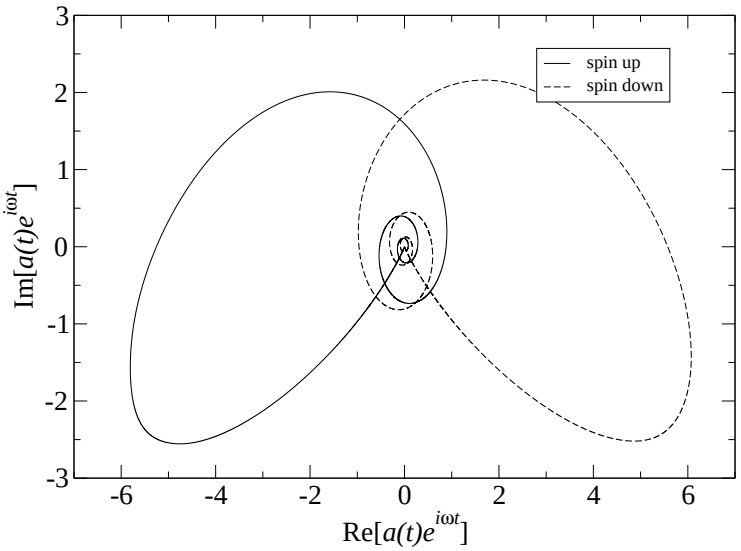

Figure 4.3: Real and imaginary part of ampltudes of the photon operator in a phase measurement as trajectories in time.

4.4.1 Phase Measurement

When a pulse of frequency $\omega_l = \omega$ is sent through the resonator, the response inside the resonator is shown in Fig. (4.1), Fig. (4.2), and Fig. (4.3). In Fig. (4.1) for the box state initially up, it starts with Rabi oscillation (the thick black line before 0.5μs) of frequency $\sqrt{\Delta^2 + g^2} \sim \Delta$, but this oscillation quickly fades away at rate κ. The dip is where the microwave pulse comes in. The photons created in the resonator by the drive mix the different states of the box as the system climbs the ladders in the dressed state picture. The maximum coherent mixing can be calculated by substituting the maximum photon number inside the resonator, ~ 40, in Fig. (4.2) into the eigenstates of the system. We get

$$|+, 40\rangle \simeq 0.96|\uparrow, 40\rangle + 0.28|\downarrow, 41\rangle, \tag{4.18}$$

$$|-, 40\rangle \simeq 0.28|\uparrow, 40\rangle - 0.96|\downarrow, 41\rangle. \tag{4.19}$$

So that the expectation value of $\langle\hat{\sigma}^z\rangle$ in the box state is

$$\langle\hat{\sigma}^z\rangle = \pm(0.96^2 - 0.28^2) \simeq \pm 0.84, \tag{4.20}$$

which corresponds to the lowest point in the upper curve and highest point in the lower curve in Fig. (4.1).

After the photons start to leak out of the resonator, *i.e* when the curve in Fig. (4.2) starts to go down, the upper curve in Fig. (4.1) goes back to its original decay route with decay rate $g^2\kappa/\Delta^2$. The revival of the box state along with the mixing effect calculated above suggest that the mixing is coherent in nature, despite the incoherent

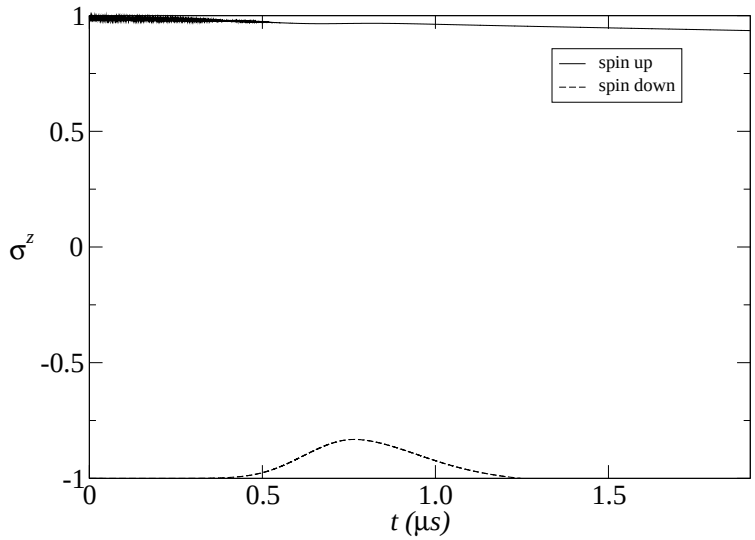

Figure 4.4: Evolution of box states in a transmission measurement with the input microwave of frequency centered on the shifted frequency corresponding to the down state.

dissipation of the resonator. This is also an evidence of the QND measurement since the final box state is shown to be unaltered by the input microwave.

Fig. (4.3) is the result of the phase measurement. The curves of spin up and spin down are mirror images about the imaginary axis, which predicts that the phases of the output signals will have the same amount of shifts with opposite signs. Since the voltage operator is proportional to $\mathrm{Re}[\langle \hat{a} \rangle]$, in the experiment this will be directly reflected in the output signal.

4.4.2 Transmission Measurement

Fig. (4.4) and Fig. (4.5) show the result of a simulation of the transmission measurement. In these graphs the frequency of the microwave pulse is centered on the lower shifted resonator frequency $\omega_l = \omega - g^2/\Delta$, which corresponds to the maximally

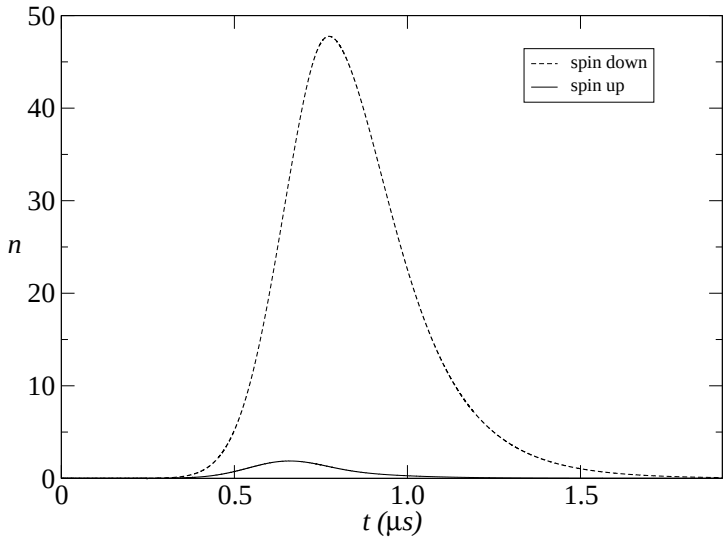

Figure 4.5: Resonator photon number in a transmission measurement with the input microwave of frequency centered on the shifted frequency corresponding to the down state.

pulled frequency when the box state is down. Fig. (4.4) and Fig. (4.1) look similar except that now the box states are less mixed for the spin up state because there are fewer photons excited in the resonator, and vice versa. In Fig. (4.5) the big contrast of resonator photon number can be seen for different box states. In the actual experimental setup, it means that the microwave pulses with the wrong frequency are mostly reflected, only those with correct frequecy can get through to be measured on the transmission line on the other side.

4.4.3 Coherent Control

One of the requirements of quantum computation is the ability to control the qubit state or to carry out one-qubit gates. This can be achieved by sending in microwave pulses with frequency $\omega_l = E_J$. Because the frequency is very far detuned from the

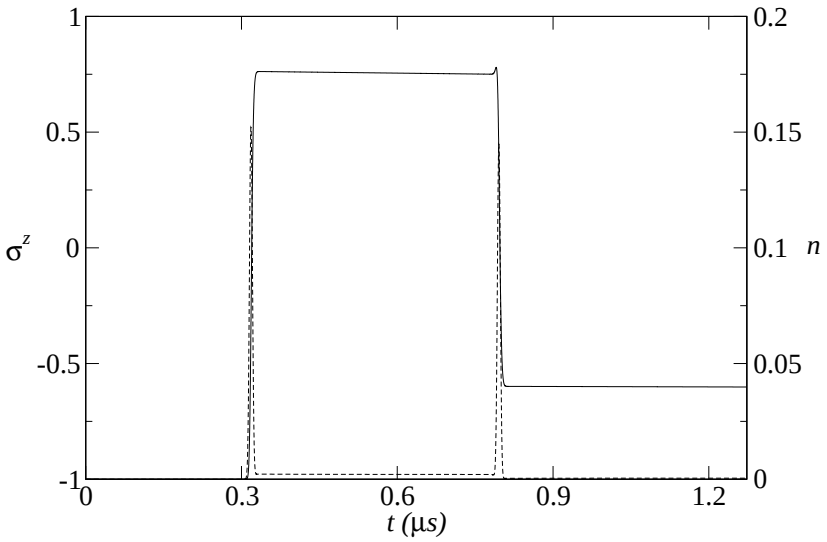

Figure 4.6: Box state and photon number under the influence of two strong but short pulses. The solid line is the state of the box with its y-axis on the left, and the dashed line is the photon number with its y-axis on the right. Notice that the number of photon excited in the resonator is less than 1. The pulse duration here is 1.2ns, and the maximum amplitude α is $2\pi \times 800$MHz.

resonator frequency, the signals are mostly filtered by the resonator, which means that the intensity of the microwave pulse must be strong enough to overcome the filtering. It is demonstrated in Fig. (4.6) that such kind of operations can be done in the qubit-resonator system. Notice that this is very different from the measurement processes where the input microwaves are near the resonator frequency, which causes strong entanglement between resonator photons and the qubit. Here the detuned microwave does not create much entanglement with the resonator. Moreover, even though the microwaves are not directly applied on the qubit, the operation is still very fast. This is due to the photons that go through the resonator being only virtual, and in the end of the operation they are completely absorbed by the qubit and leave the resonator back to its ground state.

4.4.4 Ramsey Experiment

Once the coherent control is available, by carelly choosing the intensity and duration of the pulse we can make a $\pi/2$-pulse. Then we are able to test the coherence of the qubit by a Ramsey experiment[24], which consists of two successive $\pi/2$ pulses separated by a free precessing time interval d. We can see the Ramsey fringes in Fig. (4.7). One may wonder why there is still an oscillating pattern when the pulse frequency is exactly at the box splitting E_J. This is because of the box's coupling to the resonator, which results in the Lamb shift modifying its effective energy splitting to $E_J + g^2/\Delta$, as derived in Eq. (3.18). The oscillation frequency in Fig. (4.7), which equals g^2/Δ, confirms this prediction.

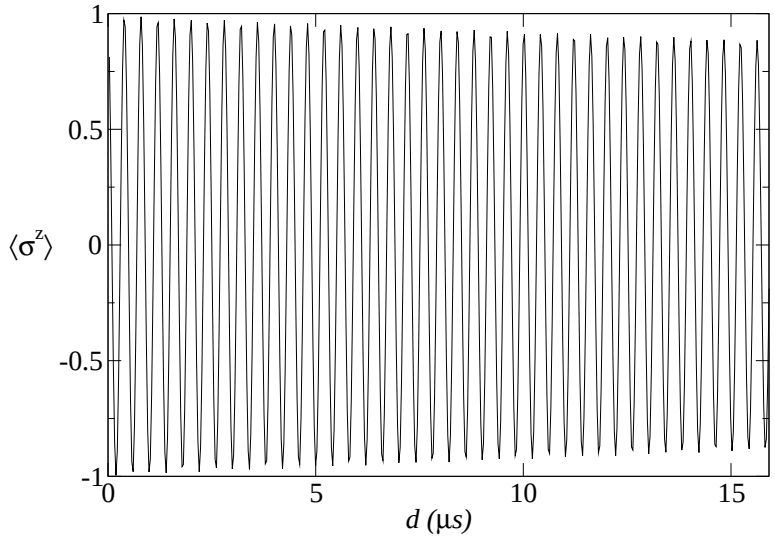

Figure 4.7: Ramsey fringes of the result of two successive $\pi/2$-pulses. d is the time interval between the two pulses. The box is initially in the $|\downarrow\rangle$ state. The frequency of the two pulses are the original box splitting E_J. The oscillation pattern decays at the rate $g^2\kappa/2\Delta^2$.

Assuming the $\pi/2$ pulses are 90° clock-wise rotations along the y-axis, that means

$$\hat{R}_{\frac{\pi}{2}} = e^{i\frac{\pi}{4}\hat{\sigma}^y} = \frac{1}{\sqrt{2}}\begin{pmatrix} 1 & 1 \\ -1 & 1 \end{pmatrix} \tag{4.21}$$

The state of the qubit initially at $|\downarrow\rangle$ undergoing a Ramsey experiment is,

$$\hat{R}_{\frac{\pi}{2}} e^{-i\hat{\mathcal{H}}d}\hat{R}_{\frac{\pi}{2}}|\downarrow\rangle = \hat{R}_{\frac{\pi}{2}} e^{-i\hat{\mathcal{H}}d}\frac{1}{\sqrt{2}}(|\uparrow\rangle + |\downarrow\rangle) = \hat{R}_{\frac{\pi}{2}}\frac{1}{\sqrt{2}}\left(e^{-i\frac{g^2}{2\Delta}d - \frac{g^2\kappa}{2\Delta^2}d}|\uparrow\rangle + e^{i\frac{g^2}{2\Delta}d}|\downarrow\rangle\right). \tag{4.22}$$

Since here everything is viewed in the rotating frame of the driving frequency ω_l, as explained above, the oscillating frequency is the difference between the driving frequency and the exact box splitting[25]. The exponential decay factor $g^2\kappa/2\Delta^2$ is half the spontaneous emmission rate and is adopted from Eq. (3.35).

The measured result is the $\hat{\sigma}^z$ expectation value of this final state,

$$\begin{aligned}
\langle\hat{\sigma}^z\rangle &= \frac{1}{\sqrt{2}}\left(\langle\uparrow|e^{i\frac{g^2}{2\Delta}d-\frac{g^2\kappa}{2\Delta^2}d}+\langle\downarrow|e^{-i\frac{g^2}{2\Delta}d}\right)\hat{R}^\dagger_{\frac{\pi}{2}}\hat{\sigma}^z\hat{R}_{\frac{\pi}{2}}\frac{1}{\sqrt{2}}\left(e^{-i\frac{g^2}{2\Delta}d-\frac{g^2\kappa}{2\Delta^2}d}|\uparrow\rangle+e^{i\frac{g^2}{2\Delta}d}|\downarrow\rangle\right)\\
&= \frac{1}{\sqrt{2}}\left(\langle\uparrow|e^{i\frac{g^2}{2\Delta}d-\frac{g^2\kappa}{2\Delta^2}d}+\langle\downarrow|e^{-i\frac{g^2}{2\Delta}d}\right)\frac{1}{\sqrt{2}}\left(e^{-i\frac{g^2}{2\Delta}d-\frac{g^2\kappa}{2\Delta^2}d}|\downarrow\rangle+e^{i\frac{g^2}{2\Delta}d}|\uparrow\rangle\right)\\
&= e^{-\frac{g^2\kappa}{2\Delta^2}d}\cos\frac{g^2d}{\Delta},
\end{aligned} \tag{4.23}$$

which exactly describes the curve in Fig. (4.7). The decay rate $g^2\kappa/2\Delta^2$ is called dephasing rate, or $1/T_2$. In this case $T_2 = 2T_1$ due to the lack of low frequency noise.

Chapter 5

Conclusion

In this dissertation the theoretical model of the qubit-resonator system was built up piece by piece. First we derived the basic Hamiltonian for the resonator and the qubit individually and then put them together. This turned out to be the well-known atom-photon interaction in cavity quantum electrodynamics, which has been studied for decades. However the difference here is that in this solid state analogy, the qubit, *i.e.* the atom, is not movable, stays inside the resonator and cannot be measured directly. This seemingly disadvantage becomes a potential asset after we discover the readout schemes based on the resonator frequency shift per qubit states, because now the resonator provides the qubit with a protection that filters out the external noises and suppresses the spontaneous emission. Whether or not this can result in a significant enhancement of the qubit lifetime remains to be seen, but at least theoretically it is an improvement.

The control of the qubit although at first seemed to suffer from the same problem that the qubit is hidden inside the resonator and cannot be controlled by sending microwaves directly from the external feed lines. The numerical simulation shows that in fact we can still manipulate the qubit through the resonator following standard

NMR techniques, only we need stronger pulses to overcome the filtering effect of the resonator.

However, to prove the system fully capable of supporting the quantum computation still requires one more stage, which is entangling multiple qubits. Here this is not covered and is left for the people who are interested. In a premature picture, we can simply place more Cooper pair boxes inside the resonator like before. Their interactions with the resonator can transport the information among different qubits and thus create the entanglement to allow quantum operations.[23] This setup poses even more questions about the readout, control, and fabrication processes. For the readout, maybe some inhomogeneities among the qubits can give different shifts of the resonator frequency that tell us the state of the qubits, and optimistically even a single shot measurement of multiple qubits! The inhomogeneities may also solve the problem for the control, but it could slow down this process because we need longer pulses to resolve different qubit energy splittings. Another thing is that here every qubit is assumed to stay close to its charge degeneracy point. Since all the qubits here share the same DC gate voltage, it could be a serious problem to tackle during the fabrication. Although this can be fixed by connecting an additional gate to each Cooper pair box, the cost is the protection provided by the resonator.

Even though the future of its application in quantum computation is still uncertain, nevertheless, we have already found many fascinating ideas along the way of studying the condensed matter analog of cavity QED. The true realization of a quantum computer may or may not be possible, but we will never know unless we have tried.

References

[1] C. Bennett, IBM Journal of Research and Development **17**, 525 (1973).

[2] P. Benioff, Journal of Statistical Physics **22**, 563 (1980).

[3] R. P. Feynman, International Journal of Theoretical Physics **21**, 467 (1982).

[4] *Quantum Theory, the Church-Turing Principle, and the Universal Quantum Computer*, vol. A400 (Royal Society of London, 1985).

[5] M. A. Nielsen, E. Knill, and R. LaFlamme, Nature **396**, 52 (1998).

[6] W. Teich, K. Obermayer, and G. Mahler, Phys. Rev. B **37**, 8111 (1988).

[7] J. I. Cirac and P. Zoller, Phys. Rev. Lett. **74**, 4091 (1995).

[8] Q. Turchette, C. Hood, C. Lange, W. Mabuchi, and H. Kimble, Phys. Rev. Lett. **75**, 4710 (1995).

[9] D. Loss and D. P. DiVincenzo, Phys. Rev. A **57**, 120 (1998).

[10] Y. Nakamura, Y. Pashkin, and J.-S. Tsai, Nature **398**, 786 (1999).

[11] M. O. Scully and M. S. Zubairy, *Quantum Optics* (Cambridge University Press, 1997).

[12] E. Merzbacher, *Quantum Mechanincs* (John Wiley & Sons, Inc., 1998), 3rd ed.

[13] C. Cohen-Tannoudji, J. Dupont-Roc, and G. Grynberg, *Atom-Photon Interactions – Basic Processes and Applications* (John Wiley & Sons, Inc., 1992).

[14] J. E. Mooij, T. P. Orlando, L. Levitov, L. Tian, C. H. van der Wal, and S. Lloyd, Science **285**, 1036 (1999).

[15] Y. Yu, S. Han, X. Chu, S.-I. Chu, and Z. Wang, Science **296**, 889 (2002).

[16] J. M. Martinis, S. Nam, and J. Aumentado, Phys. Rev. Lett. **89**, 117901 (2002).

[17] D. Vion, A. Aassime, A. Cottet, P. Joyez, H. Pothier, C. Urbina, D. Esteve, and M. H. Devoret, Science **296**, 886 (2002).

[18] M. Tinkham, *Introduction to Superconductivity* (Dover Pubns, 2004), 2nd ed.

[19] J. M. Raimond, M. Brune, and S. Haroche, Rev. Mod. Phys. **73**, 565 (2001).

[20] H. Mabuchi and A. C. Doherty, Science **298**, 1372 (2002).

[21] S. Haroche, in *Fundamental Systems in Quantum Optics*, edited by J. Dalibard, J. Raimond, and J. Zinn-Justin (Elsevier, 1992), p. 767.

[22] P. K. Day, H. G. Leduc, B. A. Mazin, A. Vayonakis, and J. Zmuidzinas, Nature **425**, 817 (2003).

[23] S. M. Girvin, R.-S. Huang, A. Blais, A. Wallraff, and R. J. Schoelkopf (2003), condmat/0310670.

[24] N. F. Ramsey, *Molecular Beams* (Oxford University Press, 1985).

[25] C. Slichter, *Principles of Magnetic Resonance* (Springer-Verlag, 1990), 3rd ed.